

---

# Can Subgraph Explanations Be Weaponized to Steal Graph Neural Networks?

---

**Ojas Nimase**

University of Southern California  
Los Angeles, USA  
nimase@usc.edu

**Jiate Li**

University of Southern California  
Los Angeles, USA  
jiateli@usc.edu

**Yue Zhao**

University of Southern California  
Los Angeles, USA  
yzhao010@usc.edu

**Yushun Dong**

Florida State University  
Tallahassee, USA  
yushun.dong@fsu.edu

## Abstract

Graph Machine Learning as a Service (GMLaaS) platforms increasingly implement explainability interfaces to meet regulatory transparency requirements. However, this transparency creates exploitable vulnerabilities for model extraction attacks. We present the first model extraction attack specifically designed for graph classification under strict black-box constraints where the attacker observes only discrete class labels and binary explanation masks (no probability scores, gradients, or confidence values). Our method (1) uses model explanation outputs to guide Monte Carlo edge sensitivity estimation toward decision boundaries, with Hoeffding concentration guarantees on estimation accuracy and (2) exploits explanation subgraphs to efficiently narrow the boundary search space. Extensive experiments on benchmark graph datasets across multiple domains demonstrate our method’s superiority over comparable baselines. These findings demonstrate that such explainability interfaces create exploitable attack surfaces, informing both defensive mechanisms and policy frameworks for explainable AI mandates. The implementation code is provided in <https://github.com/LabRAI/XSTEAL/>.

## 1 Introduction

Graph Machine Learning as a Service (GMLaaS) allows organizations to distribute access to proprietary graph-based machine learning models through publicly accessible APIs while keeping internal model workings secure [15], widely applied in applications like fraud detection [1] and recommendation systems [40, 36]. However, this paradigm faces a fundamental security threat: model extraction attacks, which reconstructs functionally similar surrogates to replicate the victim’s decision-making behavior by adversarially exploiting API access to query the inner models [35, 27, 19, 44]. This threat has motivated growing study across ML paradigms, spanning attacks, defenses, and ownership verification [33, 16, 43]. Compounding this threat, growing regulatory requirements [10, 6] and user demand [32] are pushing providers to further augment their APIs with explainability interfaces, where users would additionally be aware of the most influencing graph components on the predicted labels [41]. While such transparency mechanisms help satisfy compliance requirements, they also expose a new attack channel that fundamentally threatens the security premise GMLaaS is built upon. This fundamental tension between mandated transparency and model security has been identified as an open challenge for MLaaS [25]. This raises a critical question: can the explanations mandated for transparency be weaponized to steal the same models they explain?

Recent work has begun exploiting this vulnerability, demonstrating that explanations can enable more efficient model extraction attacks [26, 21, 18]. However, this emerging area remains sparsely studied, especially for graph neural networks. Current studies face three key limitations. **First**, existing GNN extraction methods lack a principled understanding of which training data is most effective for extraction. Current approaches construct query samples by centering on high-confidence components [26, 21, 18], but never formalize why these samples aid extraction or whether better strategies exist. Intuitively, a high-fidelity surrogate must replicate the victim’s behavior not only in high-confidence regions but also near decision boundaries where predictions change. Previous work on general (non-graph) model extraction has empirically demonstrated the effectiveness of boundary sampling [3], yet this insight has not been extended to the GNN domain where the discrete, combinatorial nature of graph data introduces fundamentally different challenges. **Second**, boundary search techniques developed for continuous domains cannot transfer to discrete graph spaces. Existing methods utilizing boundary points [3, 8] require input space continuity to efficiently locate decision boundaries. On graphs, these techniques fundamentally fail: given two graphs  $G_1, G_2$  with different predicted labels, there is no unique “midpoint” as combinatorially many graphs exist at equal edit distance from both (Figure 1) [29]. Moreover, naively estimating edge sensitivities over all  $O(n^2)$  possible edges incurs prohibitive query costs [13], compounded by the hybrid discrete-continuous nature of graph data that prevents direct application of standard optimization techniques [7, 22]. **Third**, every existing GNN extraction method requires access to rich continuous information (probability scores, continuous importance vectors, or gradient-derived signals) [21, 26, 18, 34, 45] that realistic API deployments do not provide. Under emerging regulatory mandates [10, 6], GMLaaS providers are increasingly required to furnish explanations alongside predictions. In practice, rational providers would expose the minimum information necessary for compliance (discrete class labels and binary explanation masks) rather than continuous scores or gradients that reveal additional proprietary model internals. No existing GNN extraction method operates under these minimal-information constraints.

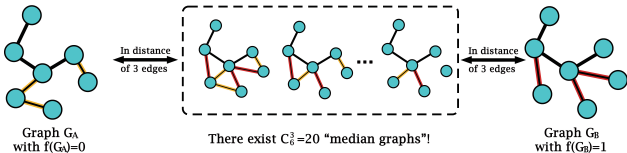


Figure 1: Multiple possible “midpoint graphs” at equal edit distance from  $G_A$  and  $G_B$ .

Our search iteratively estimates edge sensitivities via Monte Carlo sampling from discrete label responses, flips the most sensitive edges, and verifies boundary crossings. We restrict candidates to edges within or adjacent to the explanation subgraph to reduce the search space from  $O(|V|^2)$  to  $O(|V_{\text{sub}}|^2)$ . We focus on graph classification, a setting that presents unique challenges for model extraction and has not been previously addressed under strict black-box constraints. Extensive experiments across molecular, biological, and social graph benchmarks validate our framework. In summary, our contributions are:

- **Boundary Sample Effectiveness for GNNs:** We provide the first formalized definition of boundary samples for GNN extraction and empirically validate their superiority over random and high-confidence sampling strategies, recasting model extraction as a boundary pair search problem.
- **Novel Explanation-Guided Extraction Attack:** Under strict black-box constraints with only discrete predictions and binary explanation masks, we develop the first model extraction attack for graph classification that combines provably accurate Monte Carlo gradient estimation with explanation-guided candidate reduction to efficiently generate boundary samples.
- **Comprehensive Empirical Evaluation:** We conduct extensive experiments across eight graph datasets spanning molecular, biological, visual, and synthetic domains, three victim architectures, and two explainer types, demonstrating consistent superiority over adapted baselines in surrogate-victim fidelity.

## 2 Preliminaries and Motivations

**Graph Neural Networks and Explanations.** A graph  $G = (V, E, X)$  consists of nodes  $V$ , edges  $E \subseteq V \times V$ , and node features  $X \in \mathbb{R}^{|V| \times d}$ . Graph neural networks (GNNs) [14, 37, 12] process

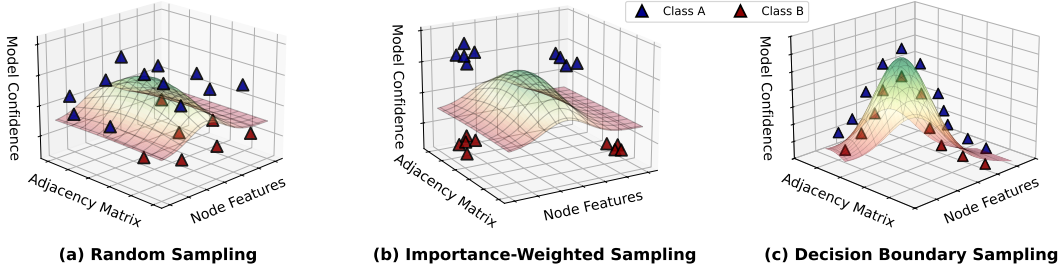


Figure 2: Sampling strategies for model extraction: surfaces are decision boundaries and triangles are classifications with smoothing for visualization clarity. Existing methods are (a) or (b), focusing on randomly sampling or sampling areas with high confidence. Our strategies are (a) and (c).

$G$  via a message passing mechanism to obtain node-level embeddings. In graph classification tasks, the GNN, denoted as  $f$ , further applies a pooling operation for a graph-level embedding, and maps the embedding to a categorical label:  $f : \mathcal{G} \rightarrow [C]$ , where  $[C] = \{1, \dots, C\}$  denotes the label space. Under the specific model  $f$  and the graph  $G$ , a GNN explainer  $h$  then returns an explanatory subgraph  $G_{\text{sub}} = (V_{\text{sub}}, E_{\text{sub}})$  where  $V_{\text{sub}} \subseteq V$  and  $E_{\text{sub}} \subseteq E$ , identifying nodes and edges most influential for the prediction  $f(G)$ . Representative methods include GNNExplainer [41] and PGExplainer [17].

**GNN Boundary Sampling Motivation.** To better address the existing gap on extraction problem formulating and answer the question we raised in Section 1: "What kind of sampling data is effective for extracting a GNN?", we investigate the effectiveness of boundary sampling on GNN extraction to solidify our motivation beforehand. We conduct a controlled experiment isolating the effect of boundary proximity on extraction fidelity across four binary benchmark datasets (AIDS, MUTAG, NCI1, Tox21\_AhR; dataset statistics are provided in Appendix E.1). Full experimental details are provided in Appendix C.

For each graph  $G$  in a shadow dataset, we exhaustively test all single edge flips ( $\delta_e = 1$ ) to identify *boundary pairs*  $(G, G')$  where  $f(G) \neq f(G')$ , and classify remaining graphs as *non-boundary samples*. We compare four training strategies on equal-sized training sets: (1) Boundary: trained exclusively on boundary pair samples, (2) Non-boundary: trained on non-boundary samples only, (3) Hybrid: trained on 50% boundary pairs + 50% random samples from the full shadow set, and (4) Shadow: trained only on random samples from the full shadow set.

Across all four datasets, surrogates with boundary data consistently outperform those without (Figure 3), confirming that decision boundary information disproportionately aids model extraction. We provide full experimental details and a theoretical analysis in Appendix C.

**Problem Formulation.** In this work we consider a *strict black-box* model extraction attack against graph neural networks. Let  $f : \mathcal{G} \rightarrow [C]$  denote a victim GNN classifier that maps graphs to discrete class labels  $[C] = \{1, \dots, C\}$ . The attacker has query access only: given any graph  $G$ , the attacker can observe the predicted label  $y(G) = f(G) \in [C]$ , but cannot access probability scores, logits, confidence values, or internal model parameters. This strict assumption reflects realistic deployment scenarios where APIs return only classification decisions.

In general model extraction attack, the attacker’s goal is to train a surrogate model  $g$  replicating the decision behavior of  $f$ , which is however uneasy to be formalized in black-box setting. Motivated by the stated effectiveness of GNN boundary samples, we instead define our problem as constructing a query set  $\mathcal{G}$  consisting of *boundary pairs*: pairs of similar graphs that receive different predictions. Formally, we aim to design an effective algorithm  $M$  to finding as much boundary pairs  $(G, G')$  as

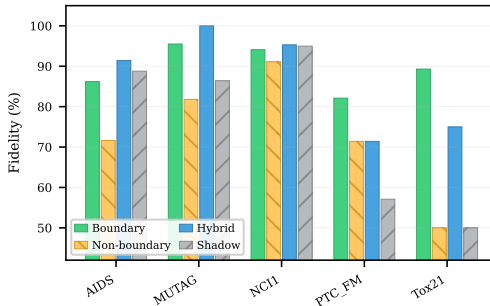


Figure 3: Fidelity (%) by sampling strategy on equal-sized training sets. Full results in Appendix Table 2.

possible, and replicate a model  $g$  trained on the pairs to rebuild the same decision boundary:

$$M(Q, f, h, \delta) = \arg \max_M |\bar{\mathcal{G}}|, \bar{\mathcal{G}} = \{(G, G') : f(G) \neq f(G') \wedge \text{dis}(G, G') \leq \delta\}$$

$$g = \arg \max_g \sum_{(G, G') \in \bar{\mathcal{G}}} \mathbb{I}(g(G) = f(G)) + \mathbb{I}(g(G') = f(G')) \quad (1)$$

$Q$  is a budget that the adversary can afford to query on the victim model.  $h$  is an GNN explainer on the holder side that returns a discrete explanatory subgraph  $G_{\text{sub}} = (V_{\text{sub}}, E_{\text{sub}})$  identifying nodes and edges important for the prediction  $f(G)$ .  $\delta > 0$  is a distance threshold and  $\text{dis}(\cdot, \cdot)$  measures graph similarity, and the distance function is defined as:  $\text{dis}(G, G') = \|A - A'\|_0$ , i.e., the number of differing entries in the adjacency matrices. We focus on structural perturbation in this work, while our later experimental evaluation empirically demonstrates that edge flips alone are sufficient for constructing our boundary search. Feature perturbation can be incorporated if needed for feature-dominated tasks. It is worth noting that a smaller  $\delta$  yields boundary pairs that more precisely characterize the local decision boundary geometry of  $f$  intuitively.

### 3 XSTEAL Framework

In this section we describe how to construct our method to search boundary pairs  $(G, G')$  satisfying the constraint in Eq. (1) using only black-box queries to the victim GNN  $f$  and its coupled explainer  $h$ . To begin with, we will firstly throw up a warm-up algorithm that serves as the background of our designed method, and briefly introduce the arising challenges along with our corresponding technique solutions as an overview. Afterwards, we will formalize these components in details.

**Warm-Up.** We notice that in convex machine learning on continuous data, it’s easy to construct a binary search method: firstly, sampling two data  $x$  and  $x'$  with different prediction results; secondly, choose the middle data point  $\frac{x+x'}{2}$  and make prediction on it; thirdly, replace  $x/x'$  with the middle point that holds the same prediction, and check if the distance of the new point pair satisfies  $\delta$ . If not, we repeat from the first step on the new pair until we reach a satisfied boundary pair.

**Challenges and Solutions.** This simple binary search is efficient and ideal, however, facing a primary challenge when practically fitting into our problem: **(C1)** in graph learning domain, even we assume the GNN model is simple as a convex model, the discrete nature of the graph data makes it impossible to find proper middle point efficiently. To address this primary challenge, we propose **(S1)** a boundary search procedure that optimizes a sample data towards decision boundary guided by the data’s local gradients. However, this requirement on gradients raised another challenge, that **(C2)** in our black-box extraction attack setting we are unable to obtain the local gradients on the victim model directly. Therefore, we accordingly propose **(S2)** a query-based Monte Carlo estimator on edge sensitivities, which approximates the local gradients by summarizing query results on the neighboring datas. While this query-based estimation gives provable accurate gradient approximation, nevertheless, it requires certain cost on queries and calculations. **(C3)** Noticing in a graph data there are  $\mathcal{O}(|V|^2)$  edges, including existent and nonexistent ones, waiting to be estimated, the query burden in total makes the estimation extremely inefficient. To further address this efficiency challenge, we refine our method with **(S3)** an explanation-guided reduction on candidate edges for query efficiency.

#### 3.1 Gradient Estimation Without Gradient Access

First, we introduce our Monte Carlo gradient estimation. Fix a base graph  $G$  and let  $G^{(t)}$  denote the current graph at iteration  $t$  of our search procedure. We write  $G^{(t)} = (A^{(t)}, X^{(t)})$  and  $y^{(t)} := y(G^{(t)})$ . Let  $y^{(0)} = y(G)$  denote the original prediction of the unperturbed graph.

**Black-box constraint.** In contrast to white-box attacks that compute  $\nabla_A \mathcal{L}$  directly, we have access only to the discrete prediction  $y(\cdot) \in [C]$ . We cannot observe probabilities, gradients, logits, or loss values. This *strict black-box* assumption reflects realistic deployment scenarios where APIs return only class labels.

**Monte Carlo gradient estimation.** To estimate the sensitivity of edge  $e$  without access to continuous outputs, we employ a Monte Carlo sampling approach. The key insight is that an edge’s

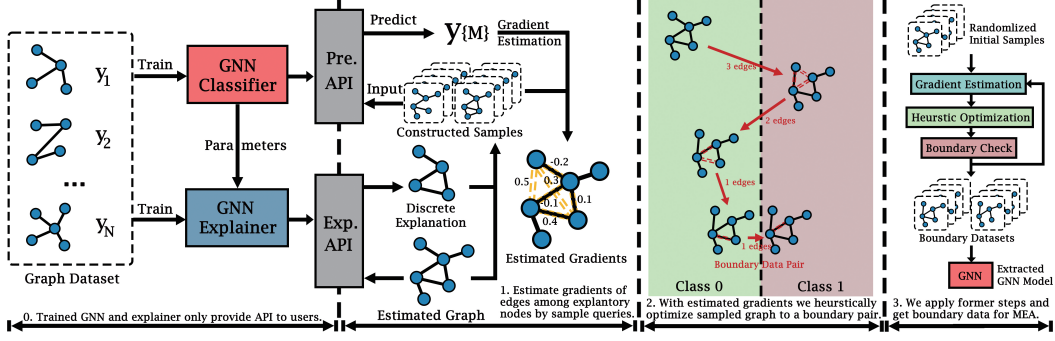


Figure 4: A visual depicting the setup of MEA and the pipeline of our proposed attack.

contribution to pushing the prediction away from  $y^{(0)}$  can be estimated by observing how often the prediction changes when that edge is present versus absent across random perturbations of the graph.

For each candidate edge  $e = (i, j) \in \mathcal{C}(G^{(t)})$ , we define the graph obtained by flipping that edge:

$$G^{(t)} \oplus e = (A^{(t)} \oplus e, X^{(t)}), \quad (2)$$

where  $A^{(t)} \oplus e$  is obtained from  $A^{(t)}$  by setting  $A_{ij}^{(t)} \leftarrow 1 - A_{ij}^{(t)}$  and  $A_{ji}^{(t)} \leftarrow 1 - A_{ji}^{(t)}$ .

For the  $m$ -th Monte Carlo sample, we generate a random perturbation  $\xi_m$  applied to edges other than  $e$ . Let  $\tilde{G}_m^{(t)}$  denote the perturbed graph with edge  $e$  in its original state, and  $\tilde{G}_m^{(t)} \oplus e$  denote the same perturbation but with edge  $e$  flipped. We define the binary observation:

$$Z_{e,m}^{(t)} = \mathbf{1}[y(\tilde{G}_m^{(t)} \oplus e) \neq y^{(0)}] - \mathbf{1}[y(\tilde{G}_m^{(t)}) \neq y^{(0)}], \quad (3)$$

where  $\mathbf{1}[\cdot]$  is the indicator function. Each  $Z_{e,m}^{(t)} \in \{-1, 0, +1\}$  measures whether flipping edge  $e$  pushes the prediction away from the original label (+1), back toward it (-1), or has no effect (0), under perturbation  $\xi_m$ . This class-agnostic formulation naturally handles both binary and multi-class settings: for binary classification it is equivalent to targeting the opposite class, while for multi-class it rewards any boundary crossing without privileging a specific target class.

We estimate the edge sensitivity by the empirical mean over  $n_e$  samples:

$$\hat{g}_e^{(t)} = \frac{1}{n_e} \sum_{m=1}^{n_e} Z_{e,m}^{(t)}. \quad (4)$$

A positive  $\hat{g}_e^{(t)}$  indicates that flipping edge  $e$  tends to push the prediction away from  $y^{(0)}$  toward a decision boundary, while a negative value suggests it reinforces the current prediction. The magnitude reflects the strength of this effect.

**Perturbation scheme.** Each perturbation  $\xi_m$  is generated by independently flipping each edge  $(i', j') \neq e$  with probability  $p_{\text{flip}} \in (0, 0.5)$ . This creates diverse graph neighborhoods around  $G^{(t)}$  while preserving the overall structure. When  $p_{\text{flip}} = 0$ , we recover the deterministic finite-difference estimate. Larger values are more robust to local decision boundary geometry, however at the cost of increased variance.

**Concentration guarantees.** Since each  $Z_{e,m}^{(t)} \in [-1, +1]$ , Hoeffding's inequality provides a concentration bound for our estimator.

**Theorem 3.1** (Hoeffding bound for edge sensitivities). *Fix an iteration  $t$  and an edge  $e \in \mathcal{C}(G^{(t)})$ . Let  $g_e^{(t)} = \mathbb{E}[Z_{e,m}^{(t)}]$  denote the true expected sensitivity and  $\hat{g}_e^{(t)}$  its empirical estimate. Then for any  $\epsilon > 0$ ,*

$$\Pr\left(|\hat{g}_e^{(t)} - g_e^{(t)}| \geq \epsilon\right) \leq 2 \exp\left(-\frac{n_e \epsilon^2}{2}\right). \quad (5)$$

Equivalently, for any confidence level  $1 - s \in (0, 1)$ , with probability at least  $1 - s$ :

$$|\hat{g}_e^{(t)} - g_e^{(t)}| \leq \sqrt{\frac{2 \log(2/s)}{n_e}}. \quad (6)$$

*Proof.* (Sketch) The binary observations  $Z_e^t$  we made under the Monte Carlo sampling are independent and all satisfy  $Z_{e,m}^t \in [-1, 1], \forall m \in [1, n_e]$ . Therefore by substituting the range  $[-1, 1]$  and  $n_e$  into Hoeffding inequality [4], we could directly reach above equations.  $\square$

The estimation error decays as  $O\left(\sqrt{\frac{1}{n_e} \log \frac{1}{s}}\right)$ , providing a formal guarantee on gradient proxy accuracy using only discrete predictions.

### 3.2 Boundary Search Via Estimated Gradients

Using the estimated sensitivities  $\{\hat{g}_e^{(t)}\}_{e \in \mathcal{C}(G^{(t)})}$ , we perform a discrete, gradient-guided search in graph space to locate decision boundaries. Since we aim to push the prediction away from the original label  $y^{(0)}$ , we select the  $k$  edges with the largest positive estimated sensitivities:

$$S^{(t)} = \text{TopK}_{\max}\left(\{\hat{g}_e^{(t)} : e \in \mathcal{C}(G^{(t)})\}, k\right), \quad (7)$$

where  $S^{(t)} \subseteq \mathcal{C}(G^{(t)})$  contains the  $k$  edges most likely to push the prediction across a decision boundary. We then update the graph by flipping all edges in  $S^{(t)}$ :  $G^{(t+1)} = \text{Update}(G^{(t)}, S^{(t)})$ , where Update applies the flip operation in Eq. (2) to each  $e \in S^{(t)}$ . Starting from  $G^{(0)} = G$ , we iterate until reaching an iteration  $t^*$  such that

$$y(G^{(t^*)}) \neq y^{(0)} \quad \text{and} \quad \delta_e(G^{(0)}, G^{(t^*)}) \leq \delta. \quad (8)$$

At this point, we record the boundary pair  $(G^{(0)}, G^{(t^*)})$ .

### 3.3 Explanation-Guided Query Reduction

Naively,  $\mathcal{C}(G^{(t)})$  could contain all possible edges, leading to  $O(|V|^2)$  queries per iteration. To make the attack query-efficient, we leverage the explanatory subgraph produced by  $h$  to restrict attention to a smaller, high-impact region of the graph.

Given  $G^{(t)}$ , we query the explainer to obtain

$$G_{\text{sub}}^{(t)} = G_{\text{sub}}(G^{(t)}) = (V_{\text{sub}}^{(t)}, E_{\text{sub}}^{(t)}, X_{\text{sub}}^{(t)}).$$

We define the one-hop neighborhood of the explanatory nodes as

$$N(V_{\text{sub}}^{(t)}) = \{j \in V(G^{(t)}) : \exists i \in V_{\text{sub}}^{(t)} \text{ with } (i, j) \in E(G^{(t)})\}.$$

We construct the candidate edge set as

$$\mathcal{C}(G^{(t)}) = \underbrace{\{(i, j) : i, j \in V_{\text{sub}}^{(t)}, i < j\}}_{\text{within-explanation edges}} \cup \underbrace{\{(i, j) : i \in V_{\text{sub}}^{(t)}, j \in N(V_{\text{sub}}^{(t)}), i < j\}}_{\text{explanation-to-neighbor edges}} \cup \underbrace{\mathcal{S}_{\text{carry}}^{(t)}}_{\text{carry-over edges}} \cup \underbrace{\mathcal{S}_{\text{rand}}^{(t)}}_{\text{random exploration}}. \quad (9)$$

Here  $\mathcal{S}_{\text{carry}}^{(t)}$  contains edges that were highly influential in previous iterations, and  $\mathcal{S}_{\text{rand}}^{(t)}$  contains randomly sampled edges for global exploration.

Since typical explanations satisfy  $|V_{\text{sub}}^{(t)}| \ll n$ , the candidate set size is

$$|\mathcal{C}(G^{(t)})| = O(|V_{\text{sub}}^{(t)}|^2 + |V_{\text{sub}}^{(t)}| \cdot d_{\text{avg}} + |\mathcal{S}_{\text{carry}}^{(t)}| + |\mathcal{S}_{\text{rand}}^{(t)}|),$$

where  $d_{\text{avg}}$  is the average degree. This reduces victim queries per iteration from  $O(|V|^2 \cdot n_e)$  to  $O(|\mathcal{C}(G^{(t)})| \cdot n_e)$ , which largely increases our method's efficiency.

To illustrate concretely, consider a typical molecular graph with  $n = 18$  nodes and an explanation subgraph of  $|V_{\text{sub}}| = 5$  nodes with average degree  $d_{\text{avg}} = 3$ . The candidate set contains  $\binom{5}{2} + 5 \cdot 3 + 5 + 10 = 40$  edges versus  $\binom{18}{2} = 153$  possible edges, a 3.8 reduction. With  $n_e = 5$  MC samples, Phase 2 requires  $\sim 400$  queries per graph per iteration versus  $\sim 1530$  naively and in practice, most graphs resolve within  $T \leq 3$  iterations.

### 3.4 Summary: Method Overview

With all above components we design, we are able to summarize our whole method in the following overview. Let  $\bar{\mathcal{G}}$  denote the set of boundary pairs obtained by applying the two-phase search procedure to all initial graphs:

$$\bar{\mathcal{G}} = \{(G, G') : y(G) \neq y(G'), \delta_e(G, G') \leq \delta\}. \quad (10)$$

We construct a training set for the surrogate model  $g$ :

$$\mathcal{D}_{\text{train}} = \{(\bar{G}, y(\bar{G})) : \forall \bar{G} \in (G, G'), (G, G') \in \bar{\mathcal{G}}\}. \quad (11)$$

The surrogate is trained via

$$\min_{g \in \mathcal{H}} \sum_{(G, y) \in \mathcal{D}_{\text{train}}} \ell(g(G), y), \quad (12)$$

where  $\mathcal{H}$  denotes the chosen GNN hypothesis class. We employ a two-phase approach. **Phase 1** cheaply tests all single-edge removals ( $O(|E(G)|)$  queries): if any removal changes the prediction, we record the boundary pair and move on; otherwise the graph passes to Phase 2. **Phase 2** triggers only when Phase 1 yields insufficient pairs, applying the full MC boundary search (Sections 3.1–3.3) to remaining graphs. This design reflects that *predictions find easy boundaries; explanations unlock hard ones*. Phase 1 is quantity-limited on low boundary-rate datasets and quality-limited on feature-dominated datasets; our phase ablation (Appendix F.4) confirms both effects. The complete algorithm is provided in Appendix D (Appendix Algorithm 1 for the overall procedure, Appendix Algorithm 2 for the BOUNDARYSEARCH subroutine).

## 4 Experiments

We evaluate our method across eight graph classification benchmarks (Table 4 in Appendix E.1), three victim architectures (GCN, GAT, GraphSAGE), and two explainer types (GNNE explainer, PGExplainer). We organize our evaluation around three research questions:

- **RQ1:** Does boundary sampling improve extraction fidelity over random and high-confidence strategies?
- **RQ2:** Does our method generalize across victim architectures and explainer types? (Appendix F.1, F.2)
- **RQ3:** How do individual components (explanation guidance, MC estimation, two-phase design) contribute to performance? (Appendix F.3, F.4)

### 4.1 Experimental Setup

We report fidelity (surrogate-victim agreement on a class-balanced test set) and accuracy (surrogate vs. ground truth). All surrogates use the same architecture family as the victim with fixed hyperparameters to isolate the effect of training data quality. Full details are in Appendix E.

**Datasets.** We evaluate on eight graph classification benchmarks spanning molecular (AIDS, MUTAG, NCI1, PTC\_FM, Tox21\_AhR), visual (MNIST, Letter-low), and synthetic (Synthie) domains. Dataset sizes range from 188 to 70,000 graphs, with five binary and three multi-class tasks (up to 15 classes), testing our method across diverse scales and decision boundary complexities. Full dataset statistics are provided in Table 4 (Appendix E.1).

**Evaluation Metrics.** We report fidelity, defined as the agreement rate between surrogate and victim predictions on a class-balanced test set. Fidelity is our primary metric because it measures how faithfully the surrogate replicates the victim’s decision logic, independent of the victim’s own correctness. We additionally report accuracy (surrogate vs. ground-truth labels) as a secondary measure. Details on test set balancing are in Appendix E.2.

**Baselines.** Existing GNN extraction attacks require either continuous victim outputs (probability scores, embeddings, or importance vectors) [34, 30, 18, 21] or operate on node classification over a shared graph [39, 45, 11]. Since no existing method operates under our discrete-only graph classification constraints, we construct baselines from straightforward strategies and adapt EGSteal [18],

Dataset	Expl.	Shadow		Non-boundary		EGSteal-BB		Boundary (XSTEAL)		Hybrid (XSTEAL)	
		Fid.	Acc.	Fid.	Acc.	Fid.	Acc.	Fid.	Acc.	Fid.	Acc.
AIDS	GNNExp	86.8±2.3	72.1±2.3	71.3±0.8	66.4±0.0	65.8±1.1	67.2±0.7	<b>91.1±0.8</b>	75.9±0.0	85.1±3.5	71.0±3.9
	PGExp					68.4±0.4	70.4±0.4	83.6±7.4	70.7±6.0	88.8±1.9	74.1±1.9
Letter-low	GNNExp	68.6±2.1	69.6±1.8	44.4±1.6	43.0±1.0	68.9±1.6	68.4±1.9	63.0±3.7	65.7±2.7	<b>72.3±0.7</b>	72.3±0.7
	PGExp					66.4±3.9	66.9±5.5	69.9±3.7	71.6±4.9	69.4±1.8	69.1±1.7
MNIST	GNNExp	53.4±1.3	26.4±0.8	48.3±2.5	24.4±0.4	53.8±1.7	26.5±0.6	54.9±2.3	26.2±0.6	<b>55.1±1.7</b>	26.6±0.4
	PGExp					50.2±0.8	25.1±0.3	52.0±2.6	25.7±0.8	53.1±3.1	25.9±0.7
MUTAG	GNNExp	81.8±3.7	68.2±3.7	84.8±2.1	65.2±2.1	90.9±0.0	68.2±0.0	<b>100.0±0.0</b>	77.3±0.0	97.0±2.1	74.2±2.1
	PGExp					90.9±0.0	68.2±0.0	<b>100.0±0.0</b>	77.3±0.0	95.5±0.0	72.7±0.0
PTC_FM	GNNExp	77.4±2.1	54.8±2.1	75.0±0.0	50.0±0.0	59.5±2.1	44.1±2.1	85.7±3.6	53.6±3.6	<b>90.5±2.1</b>	58.3±2.1
	PGExp					59.5±2.1	44.1±2.1	84.5±2.1	52.4±2.1	82.1±9.5	50.0±9.4
Synthie	GNNExp	39.7±5.5	35.3±5.0	47.4±5.5	44.2±4.2	42.9±4.0	37.8±3.3	<b>51.3±5.5</b>	44.2±4.2	46.8±3.9	40.4±6.8
	PGExp					44.9±5.0	37.8±3.3	46.2±3.1	43.6±7.4	46.2±0.0	40.4±4.2
NCI1	GNNExp	94.3±1.7	66.3±0.2	91.4±0.3	65.7±0.3	88.9±1.0	65.4±0.3	<b>96.0±0.2</b>	66.3±0.2	92.2±2.8	65.9±0.6
	PGExp					84.8±1.3	63.5±0.7	95.2±0.5	66.5±0.2	92.6±2.6	65.9±0.8
Tox21	GNNExp	60.7±5.1	54.8±6.1	54.8±3.4	48.8±3.4	54.8±3.4	48.8±3.4	89.3±2.9	83.3±4.5	77.4±9.4	76.2±7.3
	PGExp					57.1±5.8	51.2±3.4	<b>92.9±2.9</b>	82.1±2.9	91.7±1.7	80.9±1.7

Table 1: Extraction results on GCN victim at matched training set sizes. Fid. = Fidelity (%), Acc. = Accuracy (%). Best fidelity per dataset in **bold**.

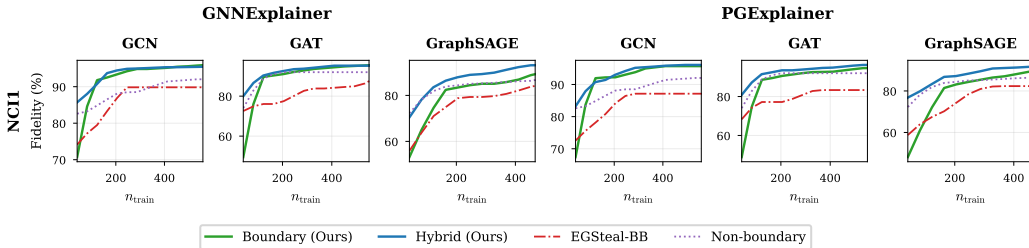


Figure 5: Fidelity (%) across increasing training set size on NCI1.

which targets the same task but under a white-box setting with continuous outputs. Our adaptation retains only its style-invariance augmentation, as the core explanation alignment mechanism requires continuous importance vectors that are unavailable in our setting. Full details are in Appendix E.10:

- **Shadow-Only:** Random shadow samples labeled by the victim, with no explanation access or boundary-seeking strategy.
- **Non-boundary:** Shadow graphs where no single-edge removal changes the victim’s prediction, representing interior-region samples far from decision boundaries.
- **EGSteal-BB:** Adaptation of EGSteal’s style-invariance augmentation to discrete explanation masks; perturbs edges outside the explanation subgraph while preserving the original label.

**Our Methods.** We evaluate two variants of our boundary-based extraction framework:

- **Boundary:** Full two-phase method (Section 3.4) combining cheap exhaustive  $\delta_e = 1$  search with explanation-guided MC boundary search.
- **Hybrid:** Allocates 50% of the query budget to boundary pair generation and 50% to random sampling, combining targeted boundary information with broad distributional coverage.

## 4.2 Main Results

In Table 1 we present extraction results on GCN victims. While in Appendix, Figure 7 visualizes fidelity across all datasets grouped by each explainer, and Figure 5 shows fidelity-vs-training-size trajectories on NCI1. Full results for GAT and GraphSAGE victims are in Appendix F.1–F.2; trajectory plots across all architectures are in Appendix G.

**RQ1: Boundary sampling improves extraction fidelity.** On all datasets, Boundary or Hybrid achieves the highest fidelity on every dataset-explainer combination, with the largest gains where baselines struggle, such like Tox21 where Boundary (92.9%) outperforms Shadow-Only (60.7%) by 32.2 points, MUTAG (100.0% vs. 81.8%), and PTC\_FM (Hybrid 90.5% vs. 77.4%). We notice non-boundary consistently underperforms, confirming interior samples alone are insufficient. Additionally,

Figure 5 shows Boundary and Hybrid separate from baselines early on NCII and converge to their advantage as training size grows. EGSteal-BB underperforms Shadow-Only on 5 of 8 datasets (GCN/GNNExplainer)—e.g., PTC\_FM: 59.5% vs. 77.4%. This notable insufficiency is consistent with its origin: EGSteal-BB is designed for white-box settings with continuous importance vectors, and our discrete adaptation necessarily strips its core alignment mechanism, leaving only style-invariance augmentation. This augmentation assumes the explanation mask causally partitions label-relevant from label-irrelevant structure; while under imprecise binary masks, this assumption breaks and the augmented samples introduce systematic label noise, which latter leads to additional fidelity loss in surrogate training (Appendix F.5).

**RQ2: Generalization across architectures and explainers.** The outperforming pattern of our methods holds across victim architectures: on GAT victims (Appendix Table 7), Boundary achieves 97.6% on Tox21 (GNNExplainer) and 95.5% on MUTAG; on GraphSAGE (Appendix Table 8), Boundary reaches 94.9% on Tox21 and 93.3% on PTC\_FM. Performance is consistent across both explainer types, with neither GNNExplainer nor PGExplainer systematically dominating. This robustness reflects a key design advantage: our method uses explanations *heuristically* to narrow the candidate edge set rather than *prescriptively* to assign labels. An imperfect explanation may degrade search *efficiency* as we would explore a suboptimal region, but not *correctness* since every boundary pair for surrogate training is verified by the victim’s own predictions.

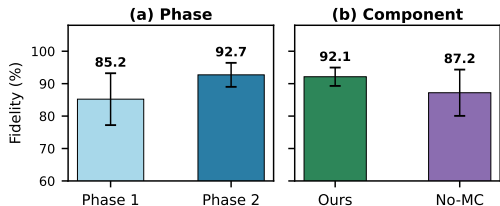


Figure 6: Phase and Component Ablations averaged across datasets and methods with error bars.

No-Exp, which only use 1 sample to estimate the sensitivity during the MC process. We first notice that No-Exp runs relatively slowly due to the high complexity, and even after running for a week we could still not get the full results. This inefficiency highlights our explanation guidance’s power on reducing estimation complexity. For the No-MC method, the component ablation (Figure 6b) shows that removing Monte Carlo sampling largely degrades its fidelity compared with ours (87.2% vs 92.1%). Moreover, we investigate No-MC’s empirical details and found in most cases the boundary search is not able to find a boundary pair till exceeding the iteration limit. The lack of sufficient boundary samples thus further leads to the de-performance. This finding highlights the necessity and effectiveness of the Monte Carlo sampling. Per-dataset breakdowns are in Appendix F.3 and F.4.

**Multi-class performance.** On multi-class datasets (Letter-low, MNIST, Synthie), Hybrid consistently outperforms pure Boundary, as boundary search fragments across multiple decision surfaces and random coverage provides complementary distributional information. Absolute fidelity on MNIST (55.1%) and Synthie (51.3%) is notably lower than on binary tasks. However, these figures should be contextualized against the number of classes: with 10 and 4 classes respectively, uniform-chance fidelity is 10% and 25%, making the achieved rates substantially above random agreement. While we notice that there is a performance gap between binary and multi-class settings, this observation is consistent with the fragmentation effect: in binary classification, all boundary pairs reinforce a single decision surface, while in multi-class settings the same query budget must be distributed across  $\binom{C}{2}$  pairwise boundaries, diluting per-surface coverage. This analysis also suggests that scaling the query budget proportionally to the number of class boundaries is a promising direction for future work.

## 5 Conclusion

In this work we answer the question posed at the start of the paper affirmatively: subgraph explanations can be weaponized to steal graph neural networks. By recasting model extraction as a boundary pair search problem, we developed the first explanation-guided model extraction attack for GNN graph classification under strict black-box constraints. Our proposed Monte Carlo edge sensitivity estimation, backed by Hoeffding concentration guarantees, enables efficient boundary pair search by restricting estimated candidates to explanation-relevant subgraph regions. Extensive experiments

across eight datasets, three victim architectures, and two explainer types demonstrate our attack’s consistent superiority over adapted baselines, with fidelity gains of up to 32 points on challenging datasets. These findings reveal a fundamental tension between regulatory demands for model transparency and the security of deployed GNN services, underscoring the need for defenses that can provide meaningful explanations without exposing decision boundary information.

## References

- [1] Amazon Web Services. Build a GNN-based real-time fraud detection solution using Amazon SageMaker, Amazon Neptune, and the Deep Graph Library. <https://aws.amazon.com/blogs/machine-learning/build-a-gnn-based-real-time-fraud-detection-solution-using-amazon-sagemaker-amazon-neptune-and-the-deep-graph-library/>, Aug. 2022.
- [2] M. Biton Dor and Y. Mirsky. Efficient model extraction via boundary sampling. In *Proceedings of the 2024 Workshop on Artificial Intelligence and Security, AISEC ’24*, page 1–11, New York, NY, USA, 2024. Association for Computing Machinery. ISBN 9798400712289. doi: 10.1145/3689932.3694756. URL <https://doi.org/10.1145/3689932.3694756>.
- [3] M. Biton Dor and Y. Mirsky. Efficient model extraction via boundary sampling. In *Proceedings of the 2024 Workshop on Artificial Intelligence and Security*, pages 1–11, 2024.
- [4] S. Boucheron, G. Lugosi, and P. Massart. *Concentration Inequalities: A Nonasymptotic Theory of Independence*. Oxford University Press, 02 2013. ISBN 9780199535255. doi: 10.1093/acprof:oso/9780199535255.001.0001. URL <https://doi.org/10.1093/acprof:oso/9780199535255.001.0001>.
- [5] Z. Cheng, B. Shen, T. Sha, Y. Gao, S. Li, and Y. Dong. Atom: A framework of detecting query-based model extraction attacks for graph neural networks, 2025. URL <https://arxiv.org/abs/2503.16693>.
- [6] Colorado General Assembly. SB24-205: Concerning Consumer Protections in Interactions with Artificial Intelligence Systems, 2024. URL <https://leg.colorado.gov/bills/sb24-205>.
- [7] H. Dai, H. Li, T. Tian, X. Huang, L. Wang, J. Zhu, and L. Song. Adversarial attack on graph structured data, 2018. URL <https://arxiv.org/abs/1806.02371>.
- [8] X. Davies, G. Giguemiani, E. Lau, E. Winsor, G. Irving, and Y. Gal. Boundary point jailbreaking of black-box llms. *arXiv preprint arXiv:2602.15001*, 2026.
- [9] V. P. Dwivedi, C. K. Joshi, A. T. Luu, T. Laurent, Y. Bengio, and X. Bresson. Benchmarking graph neural networks, 2022. URL <https://arxiv.org/abs/2003.00982>.
- [10] European Parliament and Council of the European Union. Regulation (eu) 2024/1689 laying down harmonised rules on artificial intelligence (artificial intelligence act). Official Journal of the European Union, L 2024/1689, July 2024.
- [11] F. Guan, T. Zhu, H. Tong, and W. Zhou. A realistic model extraction attack against graph neural networks. *Knowledge-Based Systems*, 300:112144, 2024. ISSN 0950-7051. doi: <https://doi.org/10.1016/j.knosys.2024.112144>. URL <https://www.sciencedirect.com/science/article/pii/S0950705124007780>.
- [12] W. L. Hamilton, R. Ying, and J. Leskovec. Inductive representation learning on large graphs, 2018. URL <https://arxiv.org/abs/1706.02216>.
- [13] R. Jin, Y. Zhou, Y. Tang, J. Song, and S. Gao. Query-efficient zeroth-order algorithms for nonconvex optimization, 2025. URL <https://arxiv.org/abs/2510.19165>.
- [14] T. N. Kipf and M. Welling. Semi-supervised classification with graph convolutional networks, 2017. URL <https://arxiv.org/abs/1609.02907>.
- [15] L. Li, B. Shen, C. Zhao, Y. Sun, K. Zhao, S. Pan, and Y. Dong. Intellectual property in graph-based machine learning as a service: Attacks and defenses, 2025. URL <https://arxiv.org/abs/2508.19641>.

- [16] Z. Li, X. Yuan, B. Shen, K. Le, H. Wang, X. Zhou, S. Gao, and Y. Dong. Query-efficient domain knowledge stealing against large language models. *Proceedings of the AAAI Conference on Artificial Intelligence*, 40(38):31870–31878, Mar. 2026. doi: 10.1609/aaai.v40i38.40456. URL <https://ojs.aaai.org/index.php/AAAI/article/view/40456>.
- [17] D. Luo, W. Cheng, D. Xu, W. Yu, B. Zong, H. Chen, and X. Zhang. Parameterized explainer for graph neural network. In H. Larochelle, M. Ranzato, R. Hadsell, M. Balcan, and H. Lin, editors, *Advances in Neural Information Processing Systems*, volume 33, pages 19620–19631. Curran Associates, Inc., 2020. URL [https://proceedings.neurips.cc/paper\\_files/paper/2020/file/e37b08dd3015330dccb5d6663667b8b8-Paper.pdf](https://proceedings.neurips.cc/paper_files/paper/2020/file/e37b08dd3015330dccb5d6663667b8b8-Paper.pdf).
- [18] B. Ma, Y. Feng, M. Lin, and E. Dai. How explanations leak the decision logic: Stealing graph neural networks via explanation alignment, 2025. URL <https://arxiv.org/abs/2506.03087>.
- [19] N. Maslej, L. Fattorini, R. Perrault, Y. Gil, V. Parli, N. Kariuki, E. Capstick, A. Reuel, E. Brynjolfsson, J. Etchemendy, K. Ligett, T. Lyons, J. Manyika, J. C. Niebles, Y. Shoham, R. Wald, T. Walsh, A. Hamrah, L. Santarlasci, J. B. Lotufo, A. Rome, A. Shi, and S. Oak. Artificial intelligence index report 2025, 2025. URL <https://arxiv.org/abs/2504.07139>.
- [20] S. Milli, L. Schmidt, A. D. Dragan, and M. Hardt. Model reconstruction from model explanations. In *Proceedings of the Conference on Fairness, Accountability, and Transparency, FAT\* '19*, page 1–9, New York, NY, USA, 2019. Association for Computing Machinery. ISBN 9781450361255. doi: 10.1145/3287560.3287562. URL <https://doi.org/10.1145/3287560.3287562>.
- [21] T. Miura, T. Shibahara, and N. Yanai. Megex: Data-free model extraction attack against gradient-based explainable ai. In *Proceedings of the 2nd ACM Workshop on Secure and Trustworthy Deep Learning Systems, SecTL '24*, page 56–66, New York, NY, USA, 2024. Association for Computing Machinery. ISBN 9798400706912. doi: 10.1145/3665451.3665533. URL <https://doi.org/10.1145/3665451.3665533>.
- [22] D. Molina-Pérez, E. A. Portilla-Flores, E. Mezura-Montes, E. Vega-Alvarado, and M. B. Calva-Yañez. Efficiently handling constraints in mixed-integer nonlinear programming problems using gradient-based repair differential evolution. *PeerJ Computer Science*, 10:e2095, May 2024. ISSN 2376-5992. doi: 10.7717/peerj-cs.2095. URL <https://doi.org/10.7717/peerj-cs.2095>.
- [23] F. Monti, D. Boscaini, J. Masci, E. Rodolà, J. Svoboda, and M. M. Bronstein. Geometric deep learning on graphs and manifolds using mixture model cnns, 2016. URL <https://arxiv.org/abs/1611.08402>.
- [24] C. Morris, N. M. Kriege, F. Bause, K. Kersting, P. Mutzel, and M. Neumann. Tudataset: A collection of benchmark datasets for learning with graphs, 2020. URL <https://arxiv.org/abs/2007.08663>.
- [25] O. Nimase, Y. Zhao, and Y. Dong. Navigating between explainability and extractability in machine learning as a service. In *2025 IEEE International Conference on Data Mining Workshops (ICDMW)*, pages 2483–2487, 2025. doi: 10.1109/ICDMW69685.2025.00305.
- [26] A. C. Oksuz, A. Halimi, and E. Ayday. Autolyucus: Exploiting explainable artificial intelligence (xai) for model extraction attacks against interpretable models. *Proceedings on Privacy Enhancing Technologies*, 2024(4):684–699, Oct. 2024. ISSN 2299-0984. doi: 10.56553/popets-2024-0137. URL <http://dx.doi.org/10.56553/popets-2024-0137>.
- [27] D. Oliynyk, R. Mayer, and A. Rauber. I know what you trained last summer: A survey on stealing machine learning models and defences. *ACM Comput. Surv.*, 55(14s), July 2023. ISSN 0360-0300. doi: 10.1145/3595292. URL <https://doi.org/10.1145/3595292>.
- [28] N. Papernot, P. McDaniel, I. Goodfellow, S. Jha, Z. B. Celik, and A. Swami. Practical black-box attacks against machine learning, 2017. URL <https://arxiv.org/abs/1602.02697>.

- [29] C. Piao, T. Xu, X. Sun, Y. Rong, K. Zhao, and H. Cheng. Computing graph edit distance via neural graph matching. *Proc. VLDB Endow.*, 16(8):1817–1829, Apr. 2023. ISSN 2150-8097. doi: 10.14778/3594512.3594514. URL <https://doi.org/10.14778/3594512.3594514>.
- [30] M. Podhajski, J. Dubiński, F. Boenisch, A. Dziedzic, A. Pregowska, and T. P. Michalak. Efficient model-stealing attacks against inductive graph neural networks, 2024. URL <https://arxiv.org/abs/2405.12295>.
- [31] K. Riesen and H. Bunke. Iam graph database repository for graph based pattern recognition and machine learning. In N. da Vitoria Lobo, T. Kasparis, F. Roli, J. T. Kwok, M. Georgiopoulos, G. C. Anagnostopoulos, and M. Loog, editors, *Structural, Syntactic, and Statistical Pattern Recognition*, pages 287–297, Berlin, Heidelberg, 2008. Springer Berlin Heidelberg. ISBN 978-3-540-89689-0.
- [32] R. Rosenbacke, Å. Melhus, M. McKee, and D. Stuckler. How explainable artificial intelligence can increase or decrease clinicians’ trust in AI applications in health care: Systematic review. *JMIR AI*, 3:e53207, 2024. doi: 10.2196/53207. URL <https://doi.org/10.2196/53207>.
- [33] B. Shen, Z. Cheng, N. Z. Gong, F. Yao, and Y. Dong. Credit: Certified ownership verification of deep neural networks against model extraction attacks, 2026. URL <https://arxiv.org/abs/2602.20419>.
- [34] Y. Shen, X. He, Y. Han, and Y. Zhang. Model stealing attacks against inductive graph neural networks, 2021. URL <https://arxiv.org/abs/2112.08331>.
- [35] F. Tramèr, F. Zhang, A. Juels, M. K. Reiter, and T. Ristenpart. Stealing machine learning models via prediction apis. In *Proceedings of the 25th USENIX Conference on Security Symposium, SEC’16*, page 601–618, USA, 2016. USENIX Association. ISBN 9781931971324.
- [36] UC Berkeley School of Information. GNNIE: GNN-recommender-as-a-service. <https://www.ischool.berkeley.edu/projects/2022/gnnie-gnn-recommender-service>, 2023.
- [37] P. Veličković, G. Cucurull, A. Casanova, A. Romero, P. Liò, and Y. Bengio. Graph attention networks, 2018. URL <https://arxiv.org/abs/1710.10903>.
- [38] Z. Wang, M. Lin, B. Shen, K. Anderson, M. Liu, T. Cai, and Y. Dong. Cega: A cost-effective approach for graph-based model extraction and acquisition, 2025. URL <https://arxiv.org/abs/2506.17709>.
- [39] B. Wu, X. Yang, S. Pan, and X. Yuan. Model extraction attacks on graph neural networks: Taxonomy and realization, 2021. URL <https://arxiv.org/abs/2010.12751>.
- [40] S. Wu, F. Sun, W. Zhang, X. Xie, and B. Cui. Graph neural networks in recommender systems: A survey. *ACM Comput. Surv.*, 55(5), Dec. 2022. ISSN 0360-0300. doi: 10.1145/3535101. URL <https://doi.org/10.1145/3535101>.
- [41] R. Ying, D. Bourgeois, J. You, M. Zitnik, and J. Leskovec. Gnnexplainer: Generating explanations for graph neural networks, 2019. URL <https://arxiv.org/abs/1903.03894>.
- [42] H. Yuan, H. Yu, J. Wang, K. Li, and S. Ji. On explainability of graph neural networks via subgraph explorations, 2021. URL <https://arxiv.org/abs/2102.05152>.
- [43] K. Zhao, L. Li, K. Ding, N. Z. Gong, Y. Zhao, and Y. Dong. A survey on model extraction attacks and defenses for large language models, 2025. URL <https://arxiv.org/abs/2506.22521>.
- [44] J. Zhou, G. Cui, S. Hu, Z. Zhang, C. Yang, Z. Liu, L. Wang, C. Li, and M. Sun. Graph neural networks: A review of methods and applications. *AI Open*, 1:57–81, 2020. ISSN 2666-6510. doi: <https://doi.org/10.1016/j.aiopen.2021.01.001>. URL <https://www.sciencedirect.com/science/article/pii/S2666651021000012>.
- [45] Y. Zhuang, C. Shi, M. Zhang, J. Chen, L. Lyu, P. Zhou, and L. Sun. Unveiling the secrets without data: can graph neural networks be exploited through data-free model extraction attacks? In *Proceedings of the 33rd USENIX Conference on Security Symposium, SEC ’24*, USA, 2024. USENIX Association. ISBN 978-1-939133-44-1.

# APPENDIX CONTENTS

<b>A Related Work</b>	<b>14</b>
<b>B Limitations and Impact Statement</b>	<b>14</b>
<b>C Boundary Sampling: Motivation and Theory</b>	<b>14</b>
C.1 Empirical Validation . . . . .	14
C.2 Theoretical Analysis of Boundary Data Effectiveness . . . . .	15
<b>D Algorithms</b>	<b>18</b>
D.1 Overall Extraction Procedure . . . . .	18
D.2 Boundary Search Subroutine . . . . .	18
<b>E Experimental Details</b>	<b>18</b>
E.1 Datasets . . . . .	18
E.2 Evaluation Metrics . . . . .	19
E.3 Victim Model Configuration . . . . .	20
E.4 Explainer Configuration . . . . .	20
E.5 Attack Configuration . . . . .	21
E.6 Surrogate Training . . . . .	21
E.7 Data Splits and Query Budget . . . . .	21
E.8 Compute Resources . . . . .	21
E.9 Implementation Notes . . . . .	21
E.10 Baseline Details . . . . .	22
<b>F Additional Results</b>	<b>22</b>
F.1 GAT Victim Results . . . . .	23
F.2 GraphSAGE Victim Results . . . . .	24
F.3 Component Ablations . . . . .	24
F.4 Phase Ablation . . . . .	25
F.5 EGSteal-BB Failure Analysis . . . . .	25
<b>G Fidelity vs. Query Budget Trajectories</b>	<b>26</b>
<b>H Query Complexity Analysis</b>	<b>27</b>

## A Related Work

**Model Extraction Attacks.** Model extraction attacks reconstruct target model functionality through query access. Early work demonstrated equation-solving attacks against simple models [35], later extended to deep neural networks [28, 20]. Recent approaches show that samples near decision boundaries maximize extraction efficiency [2]. However, most methods assume access to probability scores or confidence values, assumptions violated in realistic deployments where APIs return only discrete labels. For GNNs specifically, existing attacks target node classification [45, 34], exploiting shared graph topology and node-level embeddings. These methods fundamentally cannot transfer to graph classification, where each query involves an independent graph with only a graph-level prediction. Recent work has further explored both attack and defense strategies specific to GNN extraction [38, 5], though these also operate on node classification tasks. To our knowledge, no prior work addresses strict black-box model extraction for GNN graph classification with theoretical guarantees.

**Explanation-Guided Attacks.** Regulatory requirements such as the EU AI Act [10] increasingly mandate that MLaaS providers offer explanations, creating new attack surfaces. Methods like GNNExplainer [41], PGExplainer [17], and SubgraphX [42] identify influential substructures for predictions. Recent work demonstrates that such explanations leak exploitable information to aid model extraction attacks [26, 18]. However, these approaches either require white-box access to explanation internals or assume continuous probability outputs. In realistic GMLaaS deployments, providers return only discrete explanation outputs (important nodes/edges) via APIs and not importance scores or gradients. Our work is the first to exploit explanations under strict black-box constraints where both predictions and explanations are discrete.

## B Limitations and Impact Statement

While our work presents the first model extraction attack for GNN graph classification under strict black-box constraints, we acknowledge that no existing method operates under these same constraints. Therefore, due to the novelty of this work our baselines are necessarily adapted from methods designed for different threat models rather than direct competitors. We encourage the further development of more methods following our strict black-box constraints. Our findings demonstrate that subgraph explanations, increasingly mandated by regulations such as the EU AI Act, create exploitable attack surfaces for model extraction under strict black-box constraints. This work is intended to inform GMLaaS providers and regulators so that appropriate defenses can be developed.

## C Boundary Sampling: Motivation and Theory

### C.1 Empirical Validation

**Table Results.** Our results are outlined below, confirming the superiority of the boundary-sampling approach across all datasets.

Dataset	Boundary	Non-boundary	Hybrid	Shadow
AIDS	86.2	71.6	<b>91.4</b>	88.8
MUTAG	95.5	81.8	<b>100.0</b>	86.4
NCII	94.1	91.1	<b>95.3</b>	95.0
PTC_FM	<b>82.1</b>	71.4	71.4	57.1
Tox21_AhR	<b>89.3</b>	50.0	75.0	50.0

Table 2: Fidelity (%) on test sets with equal training set sizes. Best per dataset in **bold**.

**Data Splits.** Each dataset is split 60% victim training / 20% shadow / 20% test, stratified by class labels. The shadow set serves as the attacker’s query pool; the test set is held out for fidelity evaluation.

**Victim Models.** We train 3-layer GCN victim models via hyperparameter search over epochs  $\in \{300, 500, 700, 1000\}$  and hidden dimensions  $\in \{64, 128\}$ , selecting the configuration with highest test accuracy. This reflects a realistic threat model: a model owner naturally deploys the best-performing model, and stronger victims represent a harder extraction target. Full configurations and test accuracies across all architectures are provided in Appendix Table 5.

**Boundary Detection.** For each graph  $G$  in the shadow set, we exhaustively test all single-edge flips ( $\delta_e = 1$ ). Boundary detection statistics are reported in Table 3.

**Training Set Construction.** All four strategies (Boundary, Non-boundary, Hybrid, Shadow-Only) use equal-sized training sets, capped by the boundary pair count (the scarcest resource). Each boundary pair contributes two samples (one per class). Non-boundary and random sets are sampled to match. Hybrid uses 50% boundary + 50% random from the full shadow set.

**Surrogate Training.** Surrogates use the same 3-layer GCN architecture (hidden dim 64). Hyperparameters: learning rate 0.001, no dropout, no weight decay, batch size 8, 500 epochs, Adam optimizer. Dropout is disabled because boundary pairs are near-identical graphs with opposite labels; dropout further obscures the subtle structural differences the model must learn.

**Test Set Balancing.** Fidelity measures how well the surrogate replicates the victim’s decision logic, not merely its majority-class tendency. We evaluate on a class-balanced subset of the test set (equal samples per victim-predicted class, fixed seed). Without balancing, a surrogate predicting only the majority class achieves artificially high fidelity. Balancing ensures fidelity reflects agreement on both sides of the decision boundary.

**Boundary Detection Statistics.** Table 3 reports Phase 1 boundary detection results ( $\delta_e = 1$ ) across all datasets using GCN victims. Each boundary graph produces one pair (original + flipped) = 2 training samples. Low-rate datasets such as Tox21\_AhR rely heavily on Phase 2 for boundary pair generation.

Dataset	Shadow	Boundary	Non-Boundary	Rate
AIDS	400	127	273	31.8%
MUTAG	38	11	27	28.9%
NCI1	822	338	484	41.1%
PTC_FM	70	32	38	45.7%
Tox21_AhR	1,634	69	1,565	4.2%

Table 3: Phase 1 boundary detection results ( $\delta_e = 1$ , GCN victim).

## C.2 Theoretical Analysis of Boundary Data Effectiveness

Let  $\mathcal{H}$  be the hypothesis class of the extraction model mapping  $\mathcal{X} \rightarrow \{-1, +1\}$ . We assume the victim model  $h^* \in \mathcal{H}$  and satisfies  $L$ -Lipschitz continuity. Given a set of graph data and corresponding query responses  $\mathcal{G}_T = \{(G_t, h^*(G_t))\}$ , the victim space  $\mathcal{V}_T \subseteq \mathcal{H}$  is the set of all hypotheses consistent with the predicted graph data:

$$\mathcal{V}_T = \{h \in \mathcal{H} | h(G_t) = h^*(G_t), \forall t \in [1, \dots, T]\}$$

Besides, we define a pair of graph data  $(G, G')$  as  $\gamma$ -boundary data if their distance satisfies  $\delta_e + \delta_f = \gamma$  and they hold different queried predictions on the victim model, i.e.,  $h^*(G) \neq h^*(G')$ . We also define the disagreement region  $DIS(\mathcal{V}_T)$  as the subset of the input graph space  $\mathbb{G}$  where the surviving models in the victim space yield conflicting predictions:

$$DIS(\mathcal{V}_T) = \{G \in \mathbb{G} | \exists h_1, h_2 \in \mathcal{V}_T : h_1(G) \neq h_2(G)\}$$

For each  $h \in \mathcal{H}$ , let  $f_h : \mathbb{G} \rightarrow \mathbb{R}$  be its score function and  $h(G) = \text{sign}(f_h(G))$ . We assume every  $f_h$  is  $L$ -Lipschitz with respect to the graph distance  $d_{\mathbb{G}}(G, G') = \delta_e + \delta_f$ .

**Lemma C.1** (Boundary-pair margin constraint). *Let  $(G, G')$  be a queried  $\gamma$ -boundary pair with  $d_{\mathbb{G}}(G, G') = \gamma$  and, without loss of generality,  $h^*(G) = +1$  and  $h^*(G') = -1$ . Suppose every hypothesis  $h \in \mathcal{H}$  is induced by an  $L$ -Lipschitz score function  $f_h$ . Then any surviving hypothesis  $h \in \mathcal{V}_{T+2}$  satisfies*

$$0 < f_h(G) < L\gamma, \quad -L\gamma < f_h(G') < 0.$$

*Thus, for sufficiently small  $\gamma$ , every surviving hypothesis must place its decision boundary inside an  $O(\gamma)$  neighborhood between  $G$  and  $G'$ .*

*Proof.* Since  $h \in \mathcal{V}_{T+2}$  is consistent with the newly queried labels, we have  $h(G) = h^*(G) = +1$  and  $h(G') = h^*(G') = -1$ . Hence  $f_h(G) > 0$  and  $f_h(G') < 0$ . By  $L$ -Lipschitz continuity,

$$|f_h(G) - f_h(G')| \leq Ld_{\mathbb{G}}(G, G') = L\gamma.$$

Because  $f_h(G) > 0$  and  $f_h(G') < 0$ , we have  $f_h(G) - f_h(G') > f_h(G)$  and  $f_h(G) - f_h(G') > -f_h(G')$ . Therefore,

$$0 < f_h(G) < L\gamma, \quad -L\gamma < f_h(G') < 0. \quad \square$$

This lemma gives the local mechanism by which boundary pairs constrain the version space: a tightly coupled pair with opposite victim labels forces every surviving hypothesis to have scores close to the decision threshold at both endpoints. Consequently, hypotheses whose decision boundary does not enter an  $O(\gamma)$  neighborhood of the queried pair become inconsistent with the observed victim responses and are removed.

To give a further bound on extraction sample complexity, we define  $B(h^*, r)$  be the ball of hypotheses with an error rate of at most  $r$ ,

$$B(h^*, r) = \{h \in \mathcal{H} : \mathbb{P}_{G \sim \mathcal{D}}(h(G) \neq h^*(G)) \leq r\}.$$

and a disagreement coefficient  $\theta_{h^*}(\epsilon)$  bounds the rate of version space collapse:

$$\theta_{h^*}(\epsilon) = \sup_{r \geq \epsilon} \frac{\mathbb{P}_{G \sim \mathcal{D}}(G \in DIS(B(h^*, r)))}{r}$$

We assume that the boundary-pair sampler is non-degenerate in the following sense: at each round, the queried  $\gamma$ -boundary pairs cover the current disagreement region. More precisely, letting  $A_T = DIS(\mathcal{V}_T)$ , the marginal distribution of queried boundary endpoints dominates the conditional distribution  $\mathcal{D}(\cdot | A_T)$  up to a universal constant. This prevents the algorithm from repeatedly querying the same boundary pair and ensures that boundary queries explore the informative part of the version space.

**Theorem C.2** (Sample Complexity of Boundary Extraction). *Assume realizability,  $h^* \in \mathcal{H}$ , and suppose the boundary-pair sampler is non-degenerate: at epoch  $k$ , if  $A_k = DIS(\mathcal{V}_k)$ , the endpoint distribution  $Q_k$  of the queried boundary pairs satisfies*

$$Q_k(S) \geq c_0 \mathcal{D}(S | A_k)$$

*for every measurable  $S \subseteq A_k$  and for some constant  $c_0 > 0$ . Then, with probability at least  $1 - \delta$ , the number of queried endpoints needed to obtain a hypothesis with generalization error at most  $\epsilon$  is*

$$N = O\left(\frac{\theta_{h^*}(\epsilon)}{c_0} \left(d_{VC} \log \frac{\theta_{h^*}(\epsilon)}{c_0} + \log \frac{\log(1/\epsilon)}{\delta}\right) \log \frac{1}{\epsilon}\right).$$

*In particular, when  $c_0$  and logarithmic factors are suppressed,*

$$N = \tilde{O}\left(\theta_{h^*}(\epsilon) d_{VC} \log \frac{1}{\epsilon}\right).$$

*Counting boundary pairs instead of endpoints changes the bound only by a constant factor.*

*Proof.* Let

$$\text{err}(h) = \mathbb{P}_{G \sim \mathcal{D}}(h(G) \neq h^*(G)), \quad r_T = \max_{h \in \mathcal{V}_T} \text{err}(h).$$

Since the realizability assumption gives  $h^* \in \mathcal{V}_T$ , for any  $h \in \mathcal{V}_T$  and any graph  $G$  such that  $h(G) \neq h^*(G)$ , the graph  $G$  must belong to the disagreement region  $DIS(\mathcal{V}_T)$ . Therefore,

$$\{G : h(G) \neq h^*(G)\} \subseteq DIS(\mathcal{V}_T).$$

Moreover, by definition of  $r_T$ , we have  $\mathcal{V}_T \subseteq B(h^*, r_T)$ . Hence

$$DIS(\mathcal{V}_T) \subseteq DIS(B(h^*, r_T)).$$

By the definition of the disagreement coefficient, for any  $r_T \geq \epsilon$ ,

$$\mathbb{P}_{G \sim \mathcal{D}}(G \in DIS(\mathcal{V}_T)) \leq \mathbb{P}_{G \sim \mathcal{D}}(G \in DIS(B(h^*, r_T))) \leq \theta_{h^*}(\epsilon) r_T.$$

Denote  $\theta = \theta_{h^*}(\epsilon)$  and  $A_T = DIS(\mathcal{V}_T)$ . Consider any hypothesis  $h \in \mathcal{V}_T$  whose error is larger than  $r_T/2$ . Since its disagreement set with  $h^*$  is contained in  $A_T$ , we have

$$\mathbb{P}_{G \sim \mathcal{D}}(h(G) \neq h^*(G) \mid G \in A_T) = \frac{\mathbb{P}_{G \sim \mathcal{D}}(h(G) \neq h^*(G))}{\mathbb{P}_{G \sim \mathcal{D}}(G \in A_T)} \geq \frac{r_T/2}{\theta r_T} = \frac{1}{2\theta}.$$

Thus, conditioned on the current disagreement region, every hypothesis with error larger than  $r_T/2$  disagrees with the victim model on at least a  $1/(2\theta)$  fraction of the informative region.

Now let  $Q_T$  be the marginal distribution of queried boundary endpoints at round  $T$ . By the non-degeneracy assumption, for any measurable  $S \subseteq A_T$ ,

$$Q_T(S) \geq c_0 \mathcal{D}(S \mid A_T).$$

For any hypothesis  $h \in \mathcal{V}_T$  with  $\text{err}(h) > r_T/2$ , define

$$S_h = \{G : h(G) \neq h^*(G)\}.$$

Since  $S_h \subseteq A_T$ , the previous inequality gives

$$Q_T(S_h) \geq c_0 \mathcal{D}(S_h \mid A_T) \geq \frac{c_0}{2\theta}.$$

Therefore, under the endpoint query distribution  $Q_T$ , every hypothesis with error larger than  $r_T/2$  disagrees with the victim on a set of probability at least  $c_0/(2\theta)$ .

Apply the VC  $\epsilon$ -net theorem to the class

$$\mathcal{A} = \{\{G : h(G) \neq h^*(G)\} : h \in \mathcal{H}\},$$

whose VC dimension is  $O(d_{VC})$ . A batch of

$$m = O\left(\frac{\theta}{c_0} \left(d_{VC} \log \frac{\theta}{c_0} + \log \frac{1}{\delta_T}\right)\right)$$

queried endpoints forms an  $\epsilon$ -net for all sets in  $\mathcal{A}$  of  $Q_T$ -measure at least  $c_0/(2\theta)$  with probability at least  $1 - \delta_T$ . Hence every surviving hypothesis with error larger than  $r_T/2$  is hit by at least one queried endpoint and is eliminated. Therefore, after this batch,

$$r_{T+m} \leq \frac{r_T}{2}.$$

Starting from  $r_0 \leq 1$ , after

$$K = \left\lceil \log_2 \frac{1}{\epsilon} \right\rceil$$

epochs, the version-space radius satisfies  $r_K \leq \epsilon$ . Therefore the total number of queried boundary endpoints is

$$\begin{aligned} N &= \sum_{k=1}^K O\left(\theta_{h^*}(\epsilon) \left(d_{VC} \log \theta_{h^*}(\epsilon) + \log \frac{K}{\delta}\right)\right) \\ &= O\left(\theta_{h^*}(\epsilon) \left(d_{VC} \log \theta_{h^*}(\epsilon) + \log \frac{\log(1/\epsilon)}{\delta}\right) \log \frac{1}{\epsilon}\right). \end{aligned}$$

Suppressing logarithmic confidence factors and the mild  $\log \theta_{h^*}(\epsilon)$  term gives

$$N = O\left(\theta_{h^*} \cdot d_{VC} \log \frac{1}{\epsilon}\right).$$

Since each  $\gamma$ -boundary pair contributes two labeled endpoints, counting queries by boundary pairs only changes the bound by a constant factor. This completes the proof.  $\square$

## D Algorithms

### D.1 Overall Extraction Procedure

Algorithm 1 presents the complete XSTEAL procedure, combining Phase 1 (exhaustive search) and Phase 2 (explanation-guided MC search).

---

**Algorithm 1** XSTEAL: eXplanation-guided STEALing

---

**Require:** Victim  $f$ , explainer  $h$ , shadow set  $\mathcal{G}_{\text{shadow}}$ , edge threshold  $\delta$ , query budget  $Q$   
**Ensure:** Boundary dataset  $\bar{\mathcal{G}}$ , surrogate  $g$

```
1:  $\bar{\mathcal{G}} \leftarrow \emptyset, \mathcal{R} \leftarrow \emptyset$  //  $\mathcal{R}$ : non-boundary graphs
2: // Phase 1: exhaustive search
3: for all  $G \in \mathcal{G}_{\text{shadow}}$  do
4:   for all  $e \in E(G)$  do
5:      $G' \leftarrow G \ominus e$ 
6:     if  $y(G') \neq y(G)$  then
7:        $\bar{\mathcal{G}} \leftarrow \bar{\mathcal{G}} \cup \{(G, G')\}$ ; break
8:     end if
9:   end for
10:  if no boundary found then
11:     $\mathcal{R} \leftarrow \mathcal{R} \cup \{G\}$ 
12:  end if
13: end for
14: // Phase 2: explanation-guided MC search
15: for all  $G \in \mathcal{R}$  while  $Q > 0$  do
16:    $(G', Q_c) \leftarrow \text{BOUNDARYSEARCH}(G, f, h, \delta)$  // Alg. 2
17:    $Q = Q - Q_c$ 
18:   if  $G' \neq \text{null} \wedge Q \geq 0$  then
19:      $\bar{\mathcal{G}} \leftarrow \bar{\mathcal{G}} \cup \{(G, G')\}$ 
20:   end if
21: end for
22: Train surrogate  $g$  on  $\{(\bar{G}, f(\bar{G})) : \bar{G} \in \bar{\mathcal{G}}\}$ 
23: return  $\bar{\mathcal{G}}, g$ 
```

---

### D.2 Boundary Search Subroutine

Algorithm 2 provides the complete BOUNDARYSEARCH subroutine referenced in Algorithm 1.

## E Experimental Details

We provide the details for our experiments here. The implementation code is available at: <https://github.com/LabRAI/XSTEAL/>.

### E.1 Datasets

We evaluate on graph classification benchmarks from the TUDataset collection [24] and the GNN Benchmark suite [9], with several datasets originating from the IAM Graph Database [31]. Table 4 summarizes dataset statistics.

**Dataset Selection Rationale.** Our benchmark suite spans three key dimensions of diversity:

- **Domain diversity:** AIDS, MUTAG, NCI1, and PTC\_FM represent molecular chemistry (drug discovery and toxicity screening), Tox21\_AhR encodes toxicological assay activity (regulatory safety testing), MNIST captures handwritten digit recognition via superpixel graphs [23] (computer vision), Letter-low captures handwritten letter recognition from the IAM Graph Database [31] (computer vision), and Synthie provides a synthetic benchmark with controlled properties and rich node attributes.
- **Classification complexity:** We include five binary classification datasets (AIDS, MUTAG, NCI1, PTC\_FM, Tox21\_AhR) where a single decision boundary allows all boundary pairs to reinforce

---

**Algorithm 2** BOUNDARYSEARCH: Find boundary pair for a single graph

---

**Require:** Graph  $G$ , victim  $f$ , explainer  $h$ , edge threshold  $\Delta_e$ , max iterations  $T_{\max}$ , edges per step  $k$ , MC samples  $n_e$ , perturbation probability  $p_{\text{flip}}$ , carry-over size  $|\mathcal{S}_{\text{carry}}|$ , random exploration size  $|\mathcal{S}_{\text{rand}}|$

**Ensure:** Boundary graph  $G'$  and Query Cost  $Q_c$

```
1:  $G^{(0)} \leftarrow G, y^{(0)} \leftarrow f(G), t \leftarrow 0, \mathcal{S}_{\text{carry}} \leftarrow \emptyset$ 
2: while  $t < T_{\max}$  do
3:    $y^{(t)} \leftarrow f(G^{(t)})$ 
4:    $Q_c \leftarrow Q_c + 1$ 
5:    $\delta_e \leftarrow \|A(G^{(0)}) - A(G^{(t)})\|_0$ 
6:   if  $y^{(t)} \neq y^{(0)}$  and  $\delta_e \leq \Delta_e$  then
7:     return  $(G^{(t)}, Q_c)$ 
8:   end if
9:   if  $\delta_e \geq \Delta_e$  then
10:    break
11:   end if
12:    $G_{\text{sub}}^{(t)} \leftarrow h(G^{(t)}, y^{(t)})$  // query explainer
13:   Construct candidate edges  $\mathcal{C}(G^{(t)})$  via Eq. (9)
14:   for all  $e \in \mathcal{C}(G^{(t)})$  do
15:     Estimate  $\hat{g}_e^{(t)}$  via Eq. (4) with  $n_e$  samples
16:      $Q_c \leftarrow Q_c + n_e$ 
17:   end for
18:    $S^{(t)} \leftarrow \text{TopK}_{\max}(\{\hat{g}_e^{(t)} : \hat{g}_e^{(t)} > 0\}, k)$ 
19:   if  $S^{(t)} = \emptyset$  then
20:     break
21:   end if
22:    $G^{(t+1)} \leftarrow \text{flip edges in } S^{(t)}$  // apply Eq. (2) to each  $e \in S^{(t)}$ 
23:    $\mathcal{S}_{\text{carry}} \leftarrow \text{top-}|\mathcal{S}_{\text{carry}}| \text{ edges from } S^{(t)} \text{ by sensitivity}$ 
24:    $t \leftarrow t + 1$ 
25: end while
26: return  $(\text{null}, Q_c)$ 
```

---

Dataset	#Graphs	#Classes	Avg. $ V $	Avg. $ E $	Features
AIDS	2,000	2	15.7	16.2	38
Letter-low	2,250	15	4.7	3.1	2
MNIST	70,000	10	70.6	282.3	3
MUTAG	188	2	17.9	19.8	7
PTC_FM	349	2	14.1	14.5	14
Synthetic	400	4	95.0	172.9	15
NCII	4,110	2	29.9	32.3	37
Tox21_AhR	8,169	2	18.1	18.5	50

Table 4: Dataset statistics.

the same decision surface, and three multi-class datasets (Synthetic with 4 classes, MNIST with 10 classes, and Letter-low with 15 classes) to evaluate scalability of boundary search across increasingly complex decision boundary geometries.

- **Scale diversity:** Dataset sizes range from 188 graphs (MUTAG) to 70,000 graphs (MNIST), testing our method under both data-scarce and data-rich regimes. Graph sizes range from very small (Letter-low:  $\sim 5$  nodes, where single edge flips constitute  $\sim 30\%$  structural change) to large dense graphs (MNIST:  $\sim 71$  nodes,  $\sim 282$  edges) and large sparse graphs (Synthetic:  $\sim 95$  nodes), testing our method’s efficiency across scales. Feature representations vary from rich atom-level attributes (AIDS: 38 features, Tox21: 50 features) to minimal spatial coordinates (Letter-low: 2 features) to superpixel descriptors (MNIST: 3 features), testing robustness to feature informativeness.

## E.2 Evaluation Metrics

We report two primary metrics:

Architecture	Dataset	Hidden Dim	Selected Epochs	Test Accuracy (%)
GCN	AIDS	128	1000	87.0
	Letter-low	128	1000	86.2
	MNIST	128	200	38.1
	MUTAG	64	300	78.9
	PTC_FM	64	500	65.7
	Synthie	128	700	65.0
	NCII	64	1000	67.3
	Tox21_AhR	64	700	89.0
GAT	AIDS	128	1000	88.5
	Letter-low	64	700	98.0
	MNIST	128	500	59.6
	MUTAG	64	300	78.9
	PTC_FM	64	300	67.1
	Synthie	128	300	75.0
	NCII	64	1000	69.6
	Tox21_AhR	64	700	89.5
GraphSAGE	AIDS	128	500	90.5
	Letter-low	128	700	99.3
	MNIST	128	500	54.7
	MUTAG	64	300	76.3
	PTC_FM	64	700	64.3
	Synthie	128	1000	93.8
	NCII	128	1000	73.6
	Tox21_AhR	64	300	89.5

Table 5: Victim model configurations. Best hidden dimension and epochs selected per dataset via grid search.

- **Fidelity:** Agreement rate between surrogate and victim predictions on a class-balanced test set:  

$$\text{Fidelity} = \frac{1}{|\mathcal{D}_{\text{test}}|} \sum_{G \in \mathcal{D}_{\text{test}}} \mathbf{1}[g(G) = f(G)].$$
- **Accuracy:** Classification accuracy of the surrogate on ground-truth test labels.

Fidelity is our primary metric as it measures how faithfully the surrogate replicates the victim’s decision logic, independent of the victim’s own correctness.

### E.3 Victim Model Configuration

We employ three representative GNN architectures as victim models: Graph Convolutional Network (GCN), Graph Attention Network (GAT), and GraphSAGE. Each architecture consists of three message-passing layers followed by a global mean pooling operation and a linear classifier. We use ReLU activations and apply dropout ( $p = 0.5$ ) between layers for regularization. For each architecture-dataset combination, we perform a hyperparameter search over hidden dimensions  $\in \{64, 128\}$  and training epochs  $\in \{300, 500, 700, 1000\}$ , selecting the configuration achieving highest test accuracy. All models are trained using the Adam optimizer with learning rate 0.001, weight decay  $5e-4$ , and batch size 32. Table 5 summarizes the selected configurations and test accuracies across all architectures and datasets.

### E.4 Explainer Configuration

PGExplainer is trained on the victim model for 100 epochs with learning rate 0.003. Explanations are thresholded at the median importance score to produce binary edge masks. GNNExplainer uses 100 optimization steps per instance with node masks (`node_mask_type='object'`). Both explainer types operate on a deepcopy of the victim model to prevent gradient hooks from corrupting victim predictions during the experiment (see Appendix E.9).

## E.5 Attack Configuration

Default hyperparameters for Phase 2 (explanation-guided MC search):  $T_{\max} = 10$  (maximum iterations),  $\delta_{\max} = 20$  (maximum edge edits),  $k = 3$  (edges flipped per step),  $n_e = 5$  (Monte Carlo samples per candidate edge),  $p_{\text{flip}} = 0.05$  (perturbation probability),  $|\mathcal{S}_{\text{carry}}| = 5$  (carry-over edges from previous iteration),  $|\mathcal{S}_{\text{rand}}| = 10$  (random exploration edges per iteration). Explanation masks are thresholded at the median importance score to select important nodes/edges.

## E.6 Surrogate Training

Surrogates use the same architecture family as the victim (GCN, GAT, or GraphSAGE) with fixed hyperparameters across all methods: hidden dimension 64, 3 layers, no dropout, learning rate 0.001, 500 epochs, batch size 8, Adam optimizer. Hyperparameters are deliberately held constant to isolate the effect of training data quality—the only variable across methods is how training samples are selected and generated. This reflects realistic black-box constraints where the attacker does not know the victim’s exact configuration.

## E.7 Data Splits and Query Budget

Each dataset is split 60% victim training / 20% shadow / 20% test, stratified by class labels. The shadow set serves as the attacker’s query pool. For main results, we set the query budget to 70% of the shadow set and match all methods to the same training set size, determined by boundary pair availability (the scarcest resource). Table 6 reports the matched  $n_{\text{train}}$  for each dataset and victim architecture. This ensures fair comparison by isolating the effect of training data quality rather than quantity.

Boundary’s actual training set size ( $n_{\text{train}}$ ) may fall below the query budget when the shadow set contains insufficient boundary pairs. To ensure fair comparison, baseline methods are evaluated at the budget level yielding the closest  $n_{\text{train}}$  to Boundary’s output.

## E.8 Compute Resources

All experiments were conducted on Google Colab Pro+ using a single NVIDIA T4 GPU with high-RAM runtime. The full experimental pipeline (including victim training, boundary search, surrogate training, and evaluation across all datasets, architectures, and explainers) required approximately 600 Colab compute units.

Dataset	GCN	GAT	GraphSAGE
AIDS	280	280	280
Letter-low	122	82	116
MNIST	272	88	84
MUTAG	26	26	26
PTC_FM	48	48	48
Synthie	16	24	8
NCII	574	574	575
Tox21_AhR	384	1,142	768

Table 6: Matched training set size ( $n_{\text{train}}$ ) per dataset and victim architecture.

## E.9 Implementation Notes

**Data Generation.** Boundary and Hybrid are *generative* methods: the flipped graph in each boundary pair is a synthetic sample created by edge perturbation, not an existing shadow graph. In contrast, Shadow-Only, Non-boundary, and EGSteal-BB only relabel existing graphs from the shadow set. This data augmentation around decision boundaries is a key mechanism behind the fidelity improvement, and enables our methods to generate informative training data even on very limited shadow datasets.

**Explainer Model Isolation.** PyTorch Geometric’s explainer frameworks (GNNE explainer, PGExplainer) register forward hooks on the model that modify internal state in-place. Running an explainer

on the victim model can corrupt its predictions for subsequent queries. We resolve this by creating a copy .deepcopy of the victim model for each explainer instantiation, ensuring the original victim remains unmodified throughout the experiment.

**Test Set Balancing.** Fidelity measures how well the surrogate replicates the victim’s decision *logic*—its learned mapping from graph structure to class label—not merely its majority-class tendency. We evaluate on a class-balanced subset of the test set. Without balancing, a surrogate predicting only the majority class achieves artificially high fidelity. Balancing ensures fidelity reflects agreement on both sides of the decision boundary, with single-class prediction scoring exactly 50%.

## E.10 Baseline Details

**Shadow-Only.** Samples graphs from the shadow dataset and queries the victim for labels, with no explanation access or boundary-seeking strategy. This represents the standard model extraction baseline where training data is drawn from the attacker’s available distribution without any targeted selection.

**Non-boundary.** Trained exclusively on shadow graphs where no single-edge removal changes the victim’s prediction (identified during Phase 1). These graphs lie in the interior of decision regions, far from boundaries. This baseline tests whether interior samples alone suffice for extraction, and serves as a direct contrast to boundary-based methods.

**EGSteal-BB.** We adapt EGSteal [18] to our discrete setting. The original method requires continuous importance vectors  $E \in \mathbb{R}^{|V|}$  for rank-based explanation alignment, which is infeasible under binary masks. We retain only its style-invariance augmentation: perturbing edges outside  $G_{\text{sub}}$  while assigning the original victim label, generating 2 augmented samples per graph. This assumes  $G_{\text{sub}}$  causally determines the prediction, so style perturbations are label-preserving. When explainers produce imprecise masks, this assumption breaks down and the augmented samples introduce label noise, which can degrade fidelity below naive random sampling (see case study in Appendix F.5).

**Boundary (XSTEAL).** Our full two-phase method (Section 3.4). Phase 1 performs cheap exhaustive  $\delta_e = 1$  edge removal search; Phase 2 triggers explanation-guided MC search when Phase 1 produces insufficient pairs. Both original and flipped graphs are added to the training set with their respective victim predictions. Boundary is a *generative* method: the flipped graph in each pair is a synthetic sample created by edge perturbation, not an existing shadow graph.

**Hybrid (XSTEAL).** Allocates 50% of the query budget to boundary pair generation and 50% to random sampling. This combines the complementary strengths of both approaches: boundary pairs provide targeted information about the victim’s decision logic near class transitions, while random samples provide broad coverage of the input distribution. Hybrid mitigates the sample limitation of pure Boundary on datasets with low boundary rates.

## F Additional Results

We conduct ablations across three dimensions to assess robustness and isolate component contributions.

**Victim Architecture Ablation.** We evaluate our method across all three victim architectures to assess generalization:

- GCN [14]: Graph Convolutional Networks (main text, Table 1).
- GAT [37]: Graph Attention Networks with learned attention weights (Section F.1).
- GraphSAGE [12]: Sampling and aggregation-based architecture (Section F.2).

**Explainer Ablation.** We evaluate robustness to the explanation method deployed by the model owner by comparing two representative explainers:

- **GNNE explainer** [41]: Instance-level optimization-based explanations using node masks.
- **PGExplainer** [17]: Parameterized explainer trained across graphs using edge masks.

This ablation tests whether our method’s gains are tied to a specific explanation format or generalize across explainer types. Performance differences between explainers reflect variation in the informativeness of leaked explanation structure rather than a limitation of our method.

**Component Ablations.** We evaluate two ablations isolating key contributions of our method (Appendix F.3):

- **Boundary-NoExp:** Boundary search with *random* edge candidate selection instead of explanation-guided selection (Eq. 9). Candidate edges are sampled uniformly at random from all  $\binom{|V|}{2}$  possible edges, with the candidate set size matched to the explanation-guided set ( $|\mathcal{C}| \approx 35$ ),  $\delta_{\max} = 10$ ,  $T_{\max} = 5$ , and  $n_e = 3$  to isolate selection quality from set size. This isolates the contribution of the explainer.
- **Boundary-NoMC:** Boundary search with deterministic gradient estimation ( $n_e = 1$ ,  $p_{\text{flip}} = 0$ ) instead of Monte Carlo sampling ( $n_e = 5$ ,  $p_{\text{flip}} = 0.05$ ). This isolates the contribution of stochastic estimation.

## F.1 GAT Victim Results

Dataset	Expl.	Shadow		Non-boundary		EGSteal-BB		Boundary (XSTEAL)		Hybrid (XSTEAL)	
		Fid.	Acc.	Fid.	Acc.	Fid.	Acc.	Fid.	Acc.	Fid.	Acc.
AIDS	GNNExp	86.9	76.1	68.2	72.2	67.0	61.9	<b>89.8</b>	75.6	86.9	72.7
	PGExp					64.2	62.5	88.6	77.8	85.8	75.0
Letter-low	GNNExp	78.3	77.6	71.7	71.2	82.9	82.6	73.6	72.9	81.7	81.7
	PGExp					84.0	83.8	81.7	81.4	<b>86.0</b>	86.4
MNIST	GNNExp	33.6	27.6	36.1	29.4	35.9	28.9	28.9	24.8	33.4	27.4
	PGExp					31.6	26.4	28.5	24.5	<b>37.2</b>	30.7
MUTAG	GNNExp	81.8	68.2	86.4	63.6	86.4	72.7	<b>95.5</b>	72.7	<b>95.5</b>	72.7
	PGExp					90.9	68.2	<b>95.5</b>	72.7	<b>95.5</b>	72.7
PTC_FM	GNNExp	85.7	57.1	64.3	50.0	64.3	35.7	71.4	42.9	<b>92.9</b>	64.3
	PGExp					57.1	28.6	64.3	35.7	85.7	57.1
Synthetic	GNNExp	38.2	44.1	36.8	30.9	30.9	27.9	38.2	44.1	29.4	32.4
	PGExp					38.2	32.4	32.4	38.2	<b>39.7</b>	26.5
NCI1	GNNExp	95.0	68.0	90.8	67.7	87.2	66.5	93.2	68.3	<b>95.5</b>	69.0
	PGExp					79.5	64.0	<b>95.5</b>	69.0	93.5	68.8
Tox21	GNNExp	91.3	80.2	50.8	66.7	80.2	70.6	<b>97.6</b>	80.2	93.7	77.8
	PGExp					55.6	63.5	93.7	77.8	92.9	80.2

Table 7: Extraction results on *GAT* victim at matched training set sizes. Fid. = Fidelity (%), Acc. = Accuracy (%). Best fidelity per dataset in **bold**.

## F.2 GraphSAGE Victim Results

Dataset	Expl.	Shadow		Non-boundary		EGSteal-BB		Boundary (XSTEAL)		Hybrid (XSTEAL)	
		Fid.	Acc.	Fid.	Acc.	Fid.	Acc.	Fid.	Acc.	Fid.	Acc.
AIDS	GNNExp	88.7	75.6	72.0	74.4	70.2	65.5	84.5	75.0	83.9	76.8
	PGExp					72.0	67.3	88.7	80.4	<b>90.5</b>	79.8
Letter-low	GNNExp	<b>89.2</b>	89.0	<b>89.2</b>	89.0	86.2	85.8	88.5	88.3	<b>89.2</b>	89.0
	PGExp					88.7	88.5	85.8	85.5	81.6	81.6
MNIST	GNNExp	35.6	26.2	35.0	24.3	37.6	26.6	30.9	21.0	35.2	26.3
	PGExp					35.9	25.8	28.4	19.4	<b>39.5</b>	28.7
MUTAG	GNNExp	<b>100.0</b>	80.0	85.0	65.0	85.0	75.0	<b>100.0</b>	80.0	<b>100.0</b>	80.0
	PGExp					95.0	75.0	<b>100.0</b>	80.0	<b>100.0</b>	80.0
PTC_FM	GNNExp	73.3	60.0	63.3	63.3	53.3	46.7	83.3	50.0	90.0	56.7
	PGExp					53.3	46.7	<b>93.3</b>	53.3	86.7	53.3
Synthie	GNNExp	26.3	28.9	23.7	25.0	28.9	28.9	19.7	19.7	<b>32.9</b>	36.8
	PGExp					28.9	28.9	21.1	19.7	21.1	25.0
NCI1	GNNExp	90.2	72.1	89.2	71.4	86.2	69.8	77.6	63.2	<b>91.4</b>	72.1
	PGExp					84.5	67.0	90.4	72.0	91.0	71.4
Tox21	GNNExp	85.9	74.4	50.0	59.0	55.1	56.4	<b>94.9</b>	83.3	<b>94.9</b>	80.8
	PGExp					50.0	59.0	80.8	71.8	93.6	79.5

Table 8: Extraction results on *GraphSAGE* victim at matched training set sizes. Fid. = Fidelity (%), Acc. = Accuracy (%). Best fidelity per dataset in **bold**.

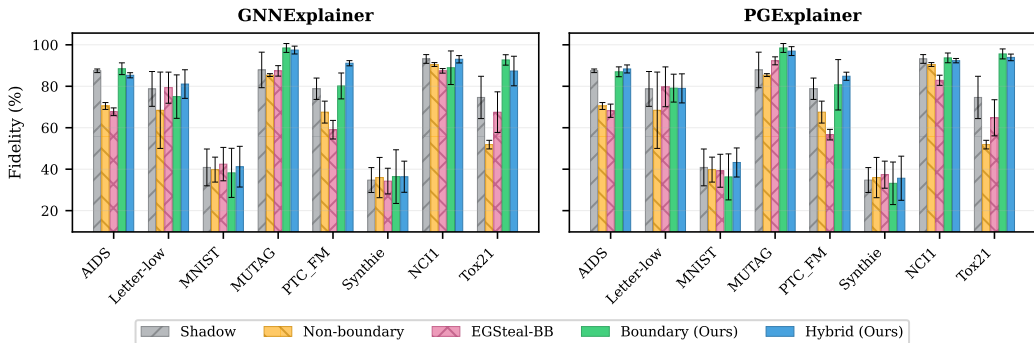


Figure 7: Extraction fidelity (%) across all architectures and datasets, grouped by explainer (left: GNNExplainer, right: PGExplainer).

## F.3 Component Ablations

Table 9 isolates the contribution of explanation guidance and Monte Carlo sampling.

Explainer	Method	AIDS		NCI1		Tox21	
		Fid.	Acc.	Fid.	Acc.	Fid.	Acc.
GNNExp.	Boundary (XSTEAL)	91.1	75.9	96.0	66.3	89.3	83.3
	Boundary-NoExp	–	–	95.5	66.1	–	–
	Boundary-NoMC	77.6	68.1	94.7	66.5	89.3	78.6

Table 9: Component ablations at 70% budget (GCN victim). Boundary-NoExp removes explanation guidance; Boundary-NoMC removes Monte Carlo sampling.

Data.	AIDS	MUTAG	NCI1	Tox21	PTC	Letter	Syn	MNIST
Fidelity	99.8%	96.8%	96.3%	99.9%	100.0%	96.7%	99.1%	93.3%

Table 11: Fidelity of the generated training data by EGSteal-BB.

#### F.4 Phase Ablation

Table 10 compares Phase 1 alone (training only on  $\delta_e = 1$  boundary pairs, capped by boundary availability) against Phase 2 alone (explanation-guided MC search on all shadow graphs) on the GCN victim for three datasets. Phase 2 outperforms Phase 1.

Dataset	Boundary		Hybrid	
	P1	P2	P1	P2
AIDS	80.2	<b>85.3</b>	85.3	<b>91.4</b>
NCI1	94.9	<b>95.2</b>	93.8	<b>95.1</b>
Tox21_AhR	71.4	<b>96.4</b>	85.7	<b>92.9</b>

Table 10: Phase ablation (GCN + GNNExp): Fidelity (%) for Phase 1 alone vs. Phase 2 alone.

#### F.5 EGSteal-BB Failure Analysis

In our general evaluation we noticed that the performance of EGSteal-BB sometimes catastrophically fail, even worse than Shadow. After further analysis, we conclude that this fail is caused by two reasons. First we note the EGSteal-BB is an adapted version for fitting our black-box model settings, and therefore removed with a few components of it which relies on the white-box settings, largely reducing its applied performance. This performance decrease validates our statement on its lack of generalization on black-box settings. Besides, we also find a partial reason, the lack of generalizability of the stated assumption on the causal relationship between the original graph and the generated graph. Specifically, in EGSteal-BB, a generated graph containing the explanation subgraph of the original graph, is assumed to always hold the same prediction as the original graph, since the subgraph is the main cause for the prediction. However, this causal assumption is based on 100% belief on a extremely accurate graph explainer, which is unlikely to happen in practical. To validate this statement, we pick out the generated graphs and compare the fidelity of its assigned label, i.e., if the victim model truly follow these labels. The results are provided as below: We additionally note that all other baselines, including our method, are training on 100% fidelity sampled datas on all datasets. Therefore, these no full fidelity causal generated datas add more fidelity loss at the training stage, which leads to its worse performance compared with other baselines.

## G Fidelity vs. Query Budget Trajectories

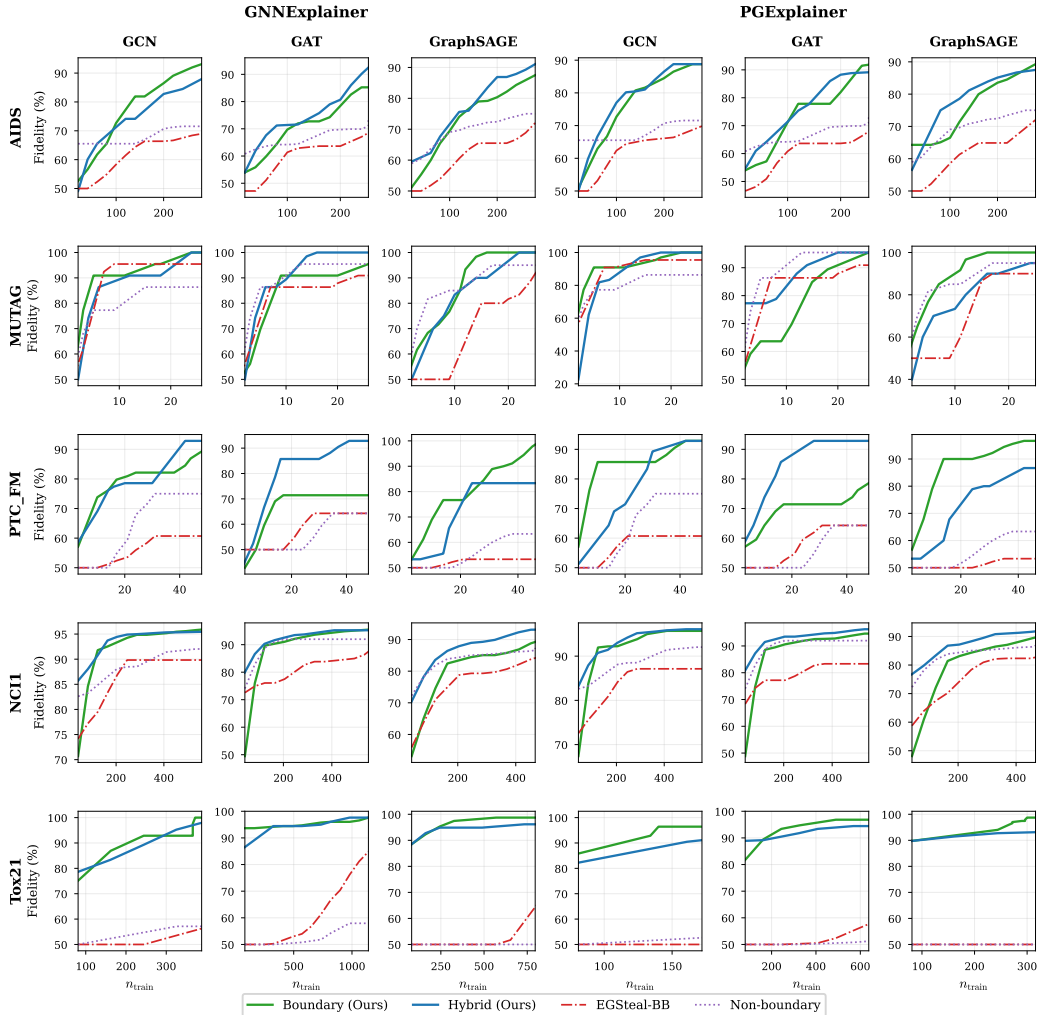


Figure 8: Fidelity (%) vs. training set size across binary datasets, victim architectures, and explainers. Rows correspond to datasets; columns to victim architectures. Top half: GNNExplainer; bottom half: PGExplainer.

Figure 8 shows surrogate fidelity as a function of training set size ( $n_{\text{train}}$ ) across all binary datasets, three victim architectures (GCN, GAT, GraphSAGE), and both explainers (top: GNNExplainer, bottom: PGExplainer).

**Setup.** For each dataset-architecture-explainer combination, we evaluate all methods at 14 training budgets from 5% to 70% of the shadow set in 5% increments. At each budget level,  $n_{\text{train}} = \lfloor |\mathcal{G}_{\text{shadow}}| \times \text{budget} \rfloor$  samples are drawn per method. Non-boundary does not use explanations; EGSteal-BB, Boundary, and Hybrid are evaluated under both GNNExplainer and PGExplainer. Fidelity trajectories apply a light smoothing (window size 3) for visualization clarity. All plots are x-axis-aligned: for each dataset-architecture-explainer triplet, the x-axis range is clipped to  $[\max(\min n_{\text{train}}), \min(\max n_{\text{train}})]$  across methods to ensure fair visual comparison.

Several patterns emerge. First, Boundary (green) and Hybrid (blue) consistently dominate across training budgets, with the gap most pronounced at small  $n_{\text{train}}$  as boundary pairs provide high-information samples that are especially valuable in low-data regimes. Second, on Tox21 (bottom row), the separation is dramatic: Boundary and Hybrid rise steeply while EGSteal-BB (red dashed)

and Non-boundary (gray dotted) remain flat near chance, reflecting Tox21’s low 4.2% boundary rate where Phase 2’s generative capacity is essential. Third, EGSteal-BB exhibits high variance and sometimes degrades with more data (e.g., AIDS/GAT, PTC\_FM/GCN), consistent with label noise from imprecise explanation masks compounding as augmented samples accumulate. Fourth, the patterns are consistent across GNNExplainer (top) and PGExplainer (bottom), confirming our method’s robustness to explainer choice.

## H Query Complexity Analysis

We analyze the number of black-box queries required to transform one initial graph  $G$  into a boundary pair  $(G, G')$ . Let  $n = |V(G)|$ , let  $k$  denote the number of edges flipped per update step, let  $n_e$  denote the number of Monte Carlo samples used to estimate each candidate edge sensitivity, and let  $\Delta_e$  be the maximum allowed edit distance between the initial graph and the returned boundary graph. At iteration  $t$ , let

$$C_t = C(G^{(t)})$$

be the explanation-guided candidate edge set, and define

$$C_{\max} = \max_{0 \leq t < T_G} |C_t|,$$

where  $T_G$  is the number of update iterations needed before the algorithm finds a boundary graph.

Since each iteration flips at most  $k$  edges, the number of update iterations is bounded by

$$T_G \leq \min \left\{ T_{\max}, \left\lceil \frac{\Delta_e}{k} \right\rceil \right\}.$$

More generally, if the first boundary crossing found by the search occurs at edit distance  $d_B(G) \leq \Delta_e$  from the initial graph, then

$$T_G \leq \left\lceil \frac{d_B(G)}{k} \right\rceil.$$

Thus, the step size  $k$  directly controls the number of search iterations: larger  $k$  reduces the number of rounds, while smaller  $k$  yields finer-grained boundary localization.

At each Phase-2 iteration, the algorithm performs one prediction query to evaluate  $y(G^{(t)})$ , one explanation query to obtain  $G_{\text{sub}}^{(t)}$ , and Monte Carlo sensitivity estimation for all edges in  $C_t$ . For each candidate edge  $e \in C_t$ , each Monte Carlo sample requires two victim prediction queries, one for  $\tilde{G}_m^{(t)}$  and one for  $\tilde{G}_m^{(t)} \oplus e$ . Therefore, the number of victim prediction queries in one Phase-2 iteration is

$$1 + 2n_e|C_t|.$$

The number of explanation queries in one Phase-2 iteration is 1.

Therefore, for a single graph entering Phase 2, the total number of victim prediction queries is bounded by

$$\begin{aligned} Q_{\text{pred}}^{(2)}(G) &\leq 1 + \sum_{t=0}^{T_G-1} (1 + 2n_e|C_t|) \\ &\leq 1 + T_G (1 + 2n_e C_{\max}) \\ &= O(T_G n_e C_{\max}). \end{aligned}$$

Substituting the step-size bound gives

$$Q_{\text{pred}}^{(2)}(G) = O \left( n_e C_{\max} \min \left\{ T_{\max}, \left\lceil \frac{\Delta_e}{k} \right\rceil \right\} \right).$$

If the successful boundary distance is  $d_B(G)$ , this can be refined to

$$Q_{\text{pred}}^{(2)}(G) = O \left( n_e C_{\max} \left\lceil \frac{d_B(G)}{k} \right\rceil \right).$$

The corresponding number of explanation queries is

$$Q_{\text{exp}}^{(2)}(G) = T_G \leq \min \left\{ T_{\max}, \left\lceil \frac{\Delta_e}{k} \right\rceil \right\}.$$

Using the explanation-guided candidate construction in Eq. (9), we have

$$C_{\max} = O(s^2 + sd_{\text{avg}} + c_{\text{carry}} + c_{\text{rand}}),$$

where

$$s = \max_t |V_{\text{sub}}^{(t)}|, \quad c_{\text{carry}} = |S_{\text{carry}}|, \quad c_{\text{rand}} = |S_{\text{rand}}|.$$

Hence the Phase-2 prediction-query complexity becomes

$$Q_{\text{pred}}^{(2)}(G) = O\left(n_e (s^2 + sd_{\text{avg}} + c_{\text{carry}} + c_{\text{rand}}) \min\left\{T_{\max}, \left\lceil \frac{\Delta_e}{k} \right\rceil\right\}\right).$$

Without explanation-guided reduction, the candidate set could contain all possible edges, giving  $C_{\max} = O(n^2)$  and therefore

$$Q_{\text{pred,naive}}^{(2)}(G) = O\left(n_e n^2 \min\left\{T_{\max}, \left\lceil \frac{\Delta_e}{k} \right\rceil\right\}\right).$$

Thus, explanation guidance reduces the per-graph Phase-2 query complexity from quadratic in the graph size to quadratic in the explanation size.

Including Phase 1, which tests all single-edge removals, the worst-case number of prediction queries for one initial graph is

$$Q_{\text{pred}}(G) \leq 1 + |E(G)| + \mathbb{I}_{\text{P2}}(G) \cdot O\left(n_e C_{\max} \min\left\{T_{\max}, \left\lceil \frac{\Delta_e}{k} \right\rceil\right\}\right),$$

where  $\mathbb{I}_{\text{P2}}(G) = 1$  if Phase 1 fails to find a boundary pair and the graph is passed to Phase 2, and  $\mathbb{I}_{\text{P2}}(G) = 0$  otherwise. Therefore, in the worst case,

$$Q_{\text{pred}}(G) = O\left(|E(G)| + n_e (s^2 + sd_{\text{avg}} + c_{\text{carry}} + c_{\text{rand}}) \min\left\{T_{\max}, \left\lceil \frac{\Delta_e}{k} \right\rceil\right\}\right).$$

This expression makes explicit the role of the step size  $k$ . Increasing  $k$  decreases the number of search iterations roughly as  $1/k$ , thereby reducing the query cost. However, larger  $k$  also makes the search less local: the returned boundary pair may lie farther from the initial graph, and the search may overshoot narrow decision-boundary regions. Conversely, smaller  $k$  requires more queries but gives finer control over the final boundary-pair distance. In practice,  $k$  therefore controls a trade-off between query efficiency and boundary-pair locality.